Additive Manufacturing 98 (2025) 104622

Contents lists available at ScienceDirect

Additive Manufacturing

journal homepage: www.elsevier.com/locate/addma

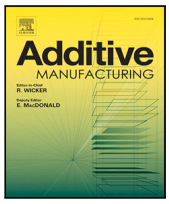

Research paper

A multi-level capture algorithm for accelerating cellular automata predictions of grain structure and texture in additive manufacturing

Xiaohui Liang [a], Jianing Zhu [a,*], Vera Popovich [a], Marcel Hermans [a], Ian Richardson [a,c], Cornelis Bos [a,b]

[a] Material Science and Engineering, TU Delft, Mekelweg 2, 2628 CD, Delft, The Netherlands
[b] Tata Steel, Research & Development, P.O. box 10000, 1970 CA IJmuiden, The Netherlands
[c] IR Welding Consultancy, Berkel en Rodenrijs, The Netherlands

ARTICLE INFO

Keywords:
Mechanistic model
Cellular automata
Additive manufacturing
Texture

ABSTRACT

Microstructure features including grain morphology and texture are key factors in determining the properties of laser additively manufactured metallic components. Beyond the traditional trial-and-error approach, which is costly and time-consuming, microstructure control increasingly relies on predictions from mechanistic models. However, existing mechanistic models to predict microstructure and texture are computationally expensive. Here, we present a cellular automata solidification model, which is up to two orders-of-magnitude faster than traditional models. By analytically calculating growth length and utilizing a multi-level capture algorithm, a large time step can be employed without compromising simulation accuracy. The model is validated through simulations of 316L steel and three NiTi cases, showing good agreement with experimental results. Our findings reveal that preferential orientations are selected by the vertical and the inclined temperature gradients from multi-pass temperature profiles, leading to different microstructures and textures. Three-dimensional additive manufacturing simulations demonstrate that orientation-dependent growth patterns govern grain growth, leading to columnar, planar and spiral shaped grains. This approach offers a significant reduction in computational cost while maintaining accuracy, contributing to the practical application of microstructure control in additive manufacturing. The insights gained on grain and texture evolution pave the way for customized microstructure design through additive manufacturing.

1. Introduction

For metallic materials, whether they are structural or functional, grain morphology and texture play vital roles in shaping properties. These microstructure features are important as they allow for the customization and optimization of various material characteristics. By carefully manipulating the grain morphology and texture, scientists and engineers can effectively enhance properties such as strength [1], conductivity [2], magnetism [3], creep resistance [4], and super-elasticity [5], among other attractive properties.

Laser powder bed fusion (LPBF), as the most adopted additive manufacturing (AM) technique for metallic components [6–8], has a unique capability for controlling microstructural features including grain morphologies and textures [9,10]. Traditionally, building AM components with desirable microstructure features has relied on trial-and-error methods, which are both costly and time-consuming [11]. Recently, the integration of advanced monitoring techniques [6,12] has enabled better control of thermal profiles, which are crucial for microstructure development. However, in-situ monitoring and control of microstructure evolution remains challenging. Due to the complexity of process conditions and high costs of experimental approaches, microstructure prediction and control increasingly relies on modeling approaches.

Computational microstructure models are valuable in a wide range of applications beyond real-time predictions. These models are useful not only for fast predictions but also for tasks like design optimization, process parameter tuning, and material selection, which can be conducted prior to manufacturing. By reducing the need for costly experimental trials, these models offer an efficient way to refine manufacturing processes. As a type of sharp-interface microstructure models, cellular automata (CA) models have been successfully used to predict microstructure evolution not only in additive manufacturing [13–17] but also in casting [18,19] and welding [20]. Nevertheless, the high computational cost of three-dimensional CA simulations poses

* Corresponding author.
E-mail address: J.Zhu-2@tudelft.nl (J. Zhu).

https://doi.org/10.1016/j.addma.2024.104622
Received 2 August 2024; Received in revised form 16 December 2024; Accepted 21 December 2024
Available online 31 December 2024

challenges for fully integrating microstructure prediction into a broader modeling framework.

Efforts to accelerate three-dimensional CA simulations have commonly involved parallelizing computations and distributing the workload across multiple processors, either in a distributed-memory or shared-memory environment. In a distributed-memory setup, each processor manages its own private memory, containing data for a portion of the simulation domain. Communication between processors is required to access data stored in another processor's memory. In such cases, an even distribution of computation tasks and corresponding data is crucial to balance the workload and optimize efficiency. For computationally intensive simulations, such as crystal plasticity simulations [21], a static decomposition method, where the domain is evenly divided among processors, typically achieves a good balance of workload and efficiency. However, CA simulations for AM present a different challenge, as most computation tasks occur near the melt pool. As the laser moves, so does the computationally intensive region, making the static decomposition method ineffective for load balancing, as indicated by Lian et al. [22]. Carozzani et al. [18] addressed this issue by using a coarse mesh, where elements are dynamically activated and assigned to processors when they are close to the melt pool. With this dynamic decomposition method, the performance of load balancing has been improved. Teferra and Rowenhorst [17] further optimized the CAFE model by first collecting the computation tasks from the entire simulation domain and redistributing them evenly across processors. However, this approach increases inter-processor communication, adding overhead, and AM simulations may still take 2 to 3 days to complete [17]. In contrast to a distributed-memory environment, a shared-memory environment allows all processors or threads to access the entire memory space, but care must be taken to prevent race conditions, where multiple threads attempt to modify the same data simultaneously. Zinovieva et al. [23] successfully implemented a CA model in a shared-memory environment to simulate the grain structure and texture of 316L steel, which align with experimental results. Despite the advantage of share-memory implementations in AM simulations, the limited memory size constrains the size of the simulation domain. Recently, with the development of GPU (Graphics Processing Unit), GPU-offloading has been a powerful technique to accelerate computationally intensive simulations. Rolchigo et al. [24–26] implemented a multi-GPU CA model, enabling the largest CA study reported in the literature. They also introduced a sparse temperature–time data format [24,26], based on the time when a cell solidifies and remelts, which reduced computational tasks and simulation time. While these studies have made significant contributions to accelerating CA simulations, due to the employed Euler forward integration method, small time steps must be employed to achieve convergence in three-dimensional simulations [24]. As indicated by Lian et al. [22], multi-capture events occur more frequently in simulations with larger time steps, resulting in substantial deviations in the simulated microstructures.

In this work, we present an improved CA model, in which the dependence on time step size has been removed by analytically calculating the growth length and employing a multi-level capture algorithm. The adoption of large time steps, combined with a pass-by-pass sparse temperature algorithm, leads to an up to two orders-of-magnitude speedup in microstructure and texture predictions without compromising simulation accuracy. The proposed CA model has been verified in directional solidification simulations, demonstrating independence on time step size. Subsequently, the current CA model is validated with a 316L AM case and three NiTi AM samples, manufactured under different conditions and having different textures. The current CA model provides fast and accurate predictions for the grain morphology and the texture of different AM samples. Furthermore, a discussion is provided on the mechanisms of texture formation and texture control during additive manufacturing.

2. Methods

In this CA model, the simulation domain is divided into several layers, aligned with the AM setup. Each AM layer is further discretized into cubic cells referenced with a cell index. Each cell has variables including grain ID, phase status (solid, liquid and interface) and the temperature at the cell center at the start and the end of the CA time step. Each interface cell also has additional variables related to growth.

2.1. Temperature calculation

To simulate AM solidification, volumetric temperature histories are necessary inputs for the CA model, which are typically obtained from analytical thermal models [17] or numerical thermal simulations with [26] and without [23] considering fluid dynamics. While analytical thermal models may be less accurate due to the use of constant material properties and failure to explicitly incorporate convection and radiation, they have the best computational efficiency and thus are employed in our CA model.

In this work, two ellipsoidal heat sources with Gaussian distributions are employed to approximate the heat input in conduction-mode or transition-mode melt pools. The analytical solution can be obtained by superimposing single ellipsoidal heat source solutions. Schwalbach et al. [27] proposed an analytical solution by approximating a moving heat source with a set of discrete heat sources. With a single moving ellipsoidal heat source, the temperature T at a point with coordinates (x, y, z) at time t is given by [27]

$$T = T_0 + f(x, y, z, t, \eta, \sigma_x, \sigma_y, \sigma_z) \tag{1}$$

with

$$f(x, y, z, t, \eta, \sigma_x, \sigma_y, \sigma_z) = \sum_{i=1}^{n} \frac{\eta P \Delta t_T}{\pi^{1.5} \rho c_p \sqrt{2\lambda_{x,i}\lambda_{y,i}\lambda_{z,i}}} \exp \left[-\frac{(x-x_i)^2}{2\lambda_{x,i}} - \frac{(y-y_i)^2}{2\lambda_{y,i}} - \frac{(z-z_i)^2}{2\lambda_{z,i}} \right] \tag{2}$$

with

$$\lambda_{q,i} = \sigma_q^2 + 2\alpha(t - \tau_i), \quad q = x, y, z, \tag{3}$$

where T_0 is the initial temperature, η the absorption efficiency of the moving heat source, P the power, ρ the density, c_p the specific heat, α the thermal diffusivity and n the number of the considered discrete heat sources. σ_x, σ_y and σ_z are shape factors of the moving heat source in the x, y and z directions, while x_i, y_i and z_i are the coordinates of the center of the ith discrete heat source. The ith heat source is activated at time τ_i and lasts for a short time period Δt_T, which is selected to ensure a smooth temperature profile. In case of two moving ellipsoidal heat sources, the temperature profile is given by

$$T = T_0 + f(x, y, z, t, \eta_1, \sigma_{x,1}, \sigma_{y,1}, \sigma_{z,1}) + f(x, y, z, t, \eta_2, \sigma_{x,2}, \sigma_{y,2}, \sigma_{z,2}). \tag{4}$$

Following Schwalbach et al. [27], $\sigma_{x,1} = \sigma_{y,1}$ and $\sigma_{x,2} = \sigma_{y,2}$ are assumed, as the laser energy distribution is circular in a plane normal to the beam. The parameters for the two moving heat sources including η_1, $\sigma_{x,1}$, $\sigma_{z,1}$, η_2, $\sigma_{x,2}$ and $\sigma_{z,2}$ are determined by fitting an averaged experimental melt pool shape. The details of the fitting procedure can be found in Section 1 in Supplementary Material.

During additive manufacturing, bidirectional laser scanning was employed in individual layers. In our CA model, a scan pattern is generated based on the hatching distance h_d and the scanning direction. At the boundary of the scan pattern, the discrete heat sources in one scan pass may influence the temperature profile in the next scan pass, leading to an enlarged melt pool. To eliminate boundary effects and simulate texture evolution in the center of the manufactured component, a padding distance is applied at the beginning and the end of each pass, which is equivalent to skywriting during real laser powder bed fusion.

2.2. Nucleation

During additive manufacturing, heterogeneous nucleation may occur due to dendrite fracture or powder particle inclusions in the melt pool, while homogeneous nucleation is less common. In prior CA models [16,28], to account for nucleation in the melt pool, the distribution function of the nucleation density n_n is modeled phenomenologically as a Gaussian distribution over the undercooling ΔT. With this phenomenological model, the columnar-to-equiaxed transition in the center of the melt pool has been successfully predicted [16]. However, the Gaussian-type nucleation model requires three parameters to be determined or fitted. Furthermore, equiaxed grains are barely observed in the studied AM samples. Hence, to reduce the number of adjustable parameters, a simpler nucleation method is employed here. Following Teferra and Rowenhorst [17], a constant nucleation density n_n is employed and nucleation is assumed to occur in the interface cells. The number of nucleation sites n_{sites} is then equal to $n_n V_{vol}$, where V_{vol} is the volume of the simulation domain. At the beginning of the simulation, a number of cells is randomly selected as nucleation sites with randomly assigned orientations. The generation of nucleation sites is controlled with a user-defined seed, which ensures that simulations are reproducible. During solidification, if a nucleation cell is captured by any interface neighbor, the nucleation cell transforms into a new interface cell with the corresponding nucleation orientation.

2.3. Growth algorithm

Following the decentered growth algorithm proposed by Gandin and Rappaz [19], each interface cell is associated with a growth octahedron with its diagonals parallel with the preferential growth direction, namely the ⟨100⟩ crystallographic direction in a cubic crystal system. The half diagonal of the growth octahedron is called growth length l and is updated in each CA time step with

$$\Delta l = l_2 - l_1 = \int_{t_1}^{t_2} v_g(\Delta T)\mathrm{d}t, \tag{5}$$

where v_g is the growth velocity, l_1 and l_2 the growth length at the start and the end of the CA time step, t_1 and t_2 the time at the start and the end of the CA time step.

The growth velocity is determined with the KGT (Kurz–Giovanola–Trivedi) model [29], which describes directional growth at a high growth rate. In the current CA model, an approximated solution [17,30,31] of the KGT model is employed, which gives the growth velocity v_g as a function of undercooling $\Delta T = T_l - T$,

$$v_g(\Delta T) = \frac{D_l \Delta T^{2.5}}{5.51\pi^2(-m_l(1-k)c_0)^{1.5}\Gamma}, \tag{6}$$

where D_l is the diffusion coefficient in the liquid, m_l the slope of the liquidus line, k the partitioning coefficient, Γ the Gibbs Thomson coefficient, c_0 the nominal concentration, T_l the liquidus temperature and T the temperature of the considered interface cell. The parameters of the studied alloy systems can be found in Section 2 in Supplementary Material.

In traditional CA models [16,17,30], the growth length change Δl in each time step is estimated with

$$\Delta l = v_g \Delta t, \tag{7}$$

where Δt is the time step. This may lead to a discretization error, especially in conditions with a high cooling rate. In the current CA model, the growth length is updated in each time step by evaluating the integral in Eq. (5) directly. Assuming the temperature and the undercooling change linearly within the considered time step, the derivative of the undercooling ΔT with respect to the time t is constant in the considered time step,

$$\frac{\mathrm{d}(\Delta T)}{\mathrm{d}t} = -\frac{T_2 - T_1}{\Delta t}. \tag{8}$$

where T_1 and T_2 are the temperature at the start and the end of the time step. Thus, the integral can be written as

$$\begin{aligned}\int_{t_1}^{t_2} v_g(\Delta T)\mathrm{d}t &= \left(\frac{\mathrm{d}(\Delta T)}{\mathrm{d}t}\right)^{-1} \int_{T_l-T_1}^{T_l-T_2} v_g(\Delta T)\mathrm{d}(\Delta T) \\ &= -\frac{\Delta t}{T_2 - T_1}\left[V_g(T_l - T_2) - V_g(T_l - T_1)\right],\end{aligned} \tag{9}$$

where V_g is the anti-derivative of the growth velocity function $v_g(\Delta T)$.

With increasing time, the growth octahedron of the considered interface cell becomes larger and captures neighboring liquid cells in the Moore neighborhood. For each neighboring liquid cell, the critical growth length l_{crit} for capture is calculated. If the growth length of the consider interface cell reaches the critical growth length l_{crit}, the corresponding liquid cell is then captured and transforms into a new interface cell. The capture time t_{cap} is calculated by solving

$$\int_{t_1}^{t_{cap}} v_g(\Delta T)\mathrm{d}t = l_{crit} - l_1. \tag{10}$$

The critical growth length l_{crit} for a growth envelope to capture a neighboring liquid cell is calculated with

$$l_{crit} = |x_r| + |y_r| + |z_r|, \tag{11}$$

where (x_r, y_r, z_r) represents the relative coordinates of the center of the considered neighboring liquid cell in a local coordinate system. This local coordinate system is defined at the center of the growth envelope, with its axes aligned along the ⟨001⟩ crystallographic directions. The relative coordinates (x_r, y_r, z_r) are determined with

$$\begin{pmatrix} x_r \\ y_r \\ z_r \end{pmatrix} = \mathbf{R}^{-1} \begin{pmatrix} x_n - x_e \\ y_n - y_e \\ z_n - z_e \end{pmatrix}, \tag{12}$$

where $\mathbf{R}$ is the rotation matrix corresponding to the crystal orientation. (x_n, y_n, z_n) denotes the global coordinates of the center of the considered liquid cell, while (x_e, y_e, z_e) represent the global coordinates of the center of the growth envelope.

After a liquid cell is transformed, a new growth octahedron is formed in the newly transformed interface cell inheriting the orientation of the parent growth octahedron. The center and the initial growth length of the new growth octahedron are determined by truncating the parent growth octahedron with the algorithm described in [19]. Note the calculation of the new growth octahedron is based on the parent octahedron at the time t_{cap}, instead of the parent octahedron at the end of the time increment t_2. After the liquid cell transforms into a new interface cell, the change in the growth length between the capture time t_{cap} and the end of the time step t_2 is calculated with

$$\Delta l = \int_{t_{cap}}^{t_2} v_g(\Delta T)\mathrm{d}t. \tag{13}$$

If all the neighboring cells in the Moore neighborhood are interface cells or solid cells, the considered interface cell then transforms into a solid cell.

2.4. Time step

The time step Δt is calculated based on the ratio between the cell size Δx and the scanning velocity v_s

$$\Delta t = \xi \frac{\Delta x}{v_s}. \tag{14}$$

In traditional CA models, ξ values including 0.024 [32], 0.04 [33], 0.1 [34], 0.2 [35] were employed to minimize the truncation error introduced by Eq. (7) and avoid a multi-capture problem, which is a problem when a liquid cell is captured by multiple interface neighbors in the same time step. The values of ξ reported in the literature includes 0.024 [32], 0.04 [33], 0.1 [34], 0.2 [35]. In the work of Lian et al. [22], when the value of ξ was increased from 0.2 to 1.0, different simulation results were obtained as the multi-capture events occur more frequently. Rolchigo et al. [24] studied the sensitivity of

grain aspect ratio to time step and indicated that $\xi \leq 0.04$ is necessary to remove the time step dependence. In the current CA model, the growth length of each interface cell is calculated analytically, which reduces the discretization error. Moreover, the capture of liquid cells occurs at specific time points. Therefore, the earliest event which transforms a cell from liquid to interface wins the competition, which then avoids the multi-capture problem. In theory, a large time step can be used in the current CA model, which reduces the total computational cost. However, another problem arises when employing a large time step $\xi \approx 1.0$. In a CA time step, after the newly captured liquid cells transform into interface cells, they can further capture their liquid neighbors in the same time step, even with $\xi < 1.0$. Thus, a multi-level capture algorithm is proposed to solve this issue in the next section.

2.5. Multi-level capture algorithm

In a CA time step, existing interface cells may capture their liquid neighbors in the Moore neighborhood at different time points. After capture, newly transformed interface cells can continue to grow and capture their liquid neighbors. For clarity, the interface cells which exist at the start of the time step are defined as level 0, while the new interface cells captured by interface cells in level i are defined as level $i + 1$. Capture trees can be constructed by denoting the interface cells and the neighboring cells they captured with nodes and connecting the parent nodes with their child nodes, as shown in Fig. 1.

In a large CA time step, a liquid cell near the solid–liquid interface could possibly be captured by multiple interface cells at different levels. Consequently, the considered liquid cell may be related to multiple capture nodes at different levels in the capture tree. The status of the considered liquid cell should be determined by the node with the shortest capture time, which does not necessarily have the smallest level number. To find the node with the shortest capture time for the considered liquid cell, it is necessary to calculate all possible capture nodes related to the considered cell. The same is true for other liquid cells near the solid–liquid interface.

To find the earliest capture node for each liquid cell near the solid–liquid interface, a direct algorithm is computing all the possible nodes within the capture trees. This can be done by performing capture checks for each newly transformed interface cell in their Moore neighborhood until no new interface cells are captured. However, this is computationally expensive. Assuming each interface cell captures 10 liquid neighbors, the time complexity of this algorithm is $\Theta(n_0 10^{N_l-1})$, where n_0 is the number of interface cells in level 0 and N_l the number of levels. As the time step increases, the number of levels increases linearly and the computational cost increases exponentially.

To reduce the computational cost, a multi-level capture algorithm is proposed, which computes the capture trees level by level and pruning is performed to reduce the computational tasks. Consider nodes at a level i. Pre-pruning is performed based on capture time and cell index of nodes in level i. A schematic illustration of the pruning conditions is shown in Fig. 1. If two or more nodes in level i correspond to the same liquid cell, only the node with the shortest capture time is allowed to have child nodes. The capture time comparison is also performed between the nodes at level i and the nodes in previous levels. If the considered node at level i is later than any node in previous layers and they are related to the same cell, then the considered node at level i is not allowed to have child nodes, which is considered as pre-pruning. If the considered node at level i is earlier than a node at a level j ($j < i$) and they are related to the same liquid cell, then the node at level j is invalid. If the invalid node at level j has descendants, then its descendant nodes are also invalid and will be removed from the capture trees. This operation is called post-pruning as pruning is performed after the calculation of the descendant of the invalid nodes. The level-by-level iterations continue until no new liquid cells are captured. The complexity level for this algorithm is approximately $\Theta(26 n_0 N_l)$ if we assume the number of nodes in each layer is similar. The pseudocode of the multi-level capture algorithm can be found in section 3 in Supplementary Material.

2.6. Pass-by-pass sparse temperature algorithm

In a CA simulation, temperature calculation is required for two purposes: one is to melt the cells in the front of the moving melt pool and the other is to determine undercooling for undercooled cells in the tail of the melt pool. Both are near the melt pool. Consequently, calculating temperature for all cells in the simulation domain is computationally expensive and unnecessary. Rolchigo et al. [24,25] proposed a sparse temperature data format based on the final time when each cell solidifies and reduced the computation cost. However, it may lead to inaccurate calculations in regions where the material solidifies and remelts several times, especially when the scanning direction rotates for each layer. Rolchigo et al. [26] introduced the concept of "temporary solid cells" to address the remelting issue in a multi-pass layer and further reduced the computational tasks by restricting calculations to undercooled interface cells. In this work, instead of collecting sparse temperature data for all the passes of the current layer [26], the sparse temperature data of each cell is updated at the beginning of each laser pass. For each cell, the maximum temperature in the current pass is computed. If the maximum temperature of a CA cell exceeds the liquidus temperature T_l, the phase of this CA cell is set to liquid, thus avoiding melting checks in subsequent CA steps within that laser pass. Additionally, the time at which each liquid cell becomes undercooled is calculated and stored, allowing for explicit tracking of the set of undercooled cells in subsequent time steps. In these time steps, due to the efficiency of the analytical thermal model, the temperature of each undercooled cell is updated precisely with Eq. (2) and (4), rather than relying on a cooling rate approximation as in previous works [24,26]. Nucleation and growth are performed in undercooled cells based on updated temperature. At the end of each passes, all cells transform into solid cells.

2.7. Parallelism and memory management

In this work, the simulation is parallelized using OpenMP (multiprocessing) with C++ in a shared memory environment. The simulation data is saved in a shared memory space which is accessible for all the processors. Therefore, in each CA step, computational tasks like temperature calculation for undercooled liquid cells and capture check for interface cells can be equally assigned to all the processors without a large overhead. Thus, it is easier to balance the loads among all the processors compared to a distributed memory environment. For tasks such as temperature calculation and growth length updates, no race conditions are encountered. For operations that involve adding or removing interface cells from the main container, serial operations are employed. In the implementation of the multi-level capture algorithm, the capture check for each level is parallelized using multi-threading, with each thread assigned a thread-local container. This approach effectively avoids race conditions.

In a CA simulation, saving the data of all the cells in the simulation domain requires a large memory space. However, this is not necessary. During additive manufacturing, melting and solidification only occur in a few layers in the upper region. Therefore, the memory requirement can be reduced by only saving data of cells in the upper layers in the memory. In this work, the data of all cells are stored layer-by-layer on the hard disk in a HDF5 [36] file, which has a good performance in input/output performance. At the beginning of the simulation, a number of layers are loaded into the memory for simulation. During the simulation, if a new layer needs to be added, the data of the bottom layer will be dumped from the memory to the hard disk and the data of the new layer will be loaded. Consequently, the number of layers in the memory is constant throughout the simulation. The number of layers in the memory should be selected based on the depth of the melt pool to avoid a complete penetration. The cost of data transfer between the memory and the hard disk is insignificant compared to the computation cost.

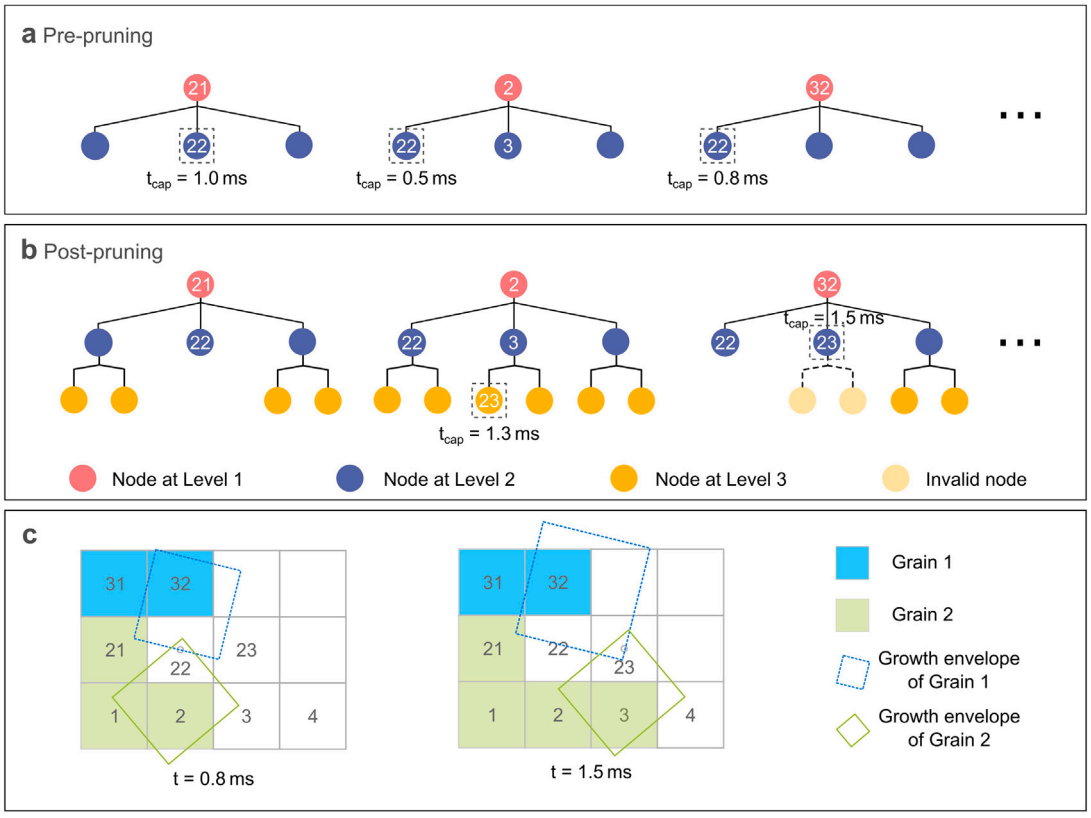

Fig. 1. A schematic illustration of the pruning conditions in the multi-level capture algorithm. Capture trees are constructed by denoting the interface cells and the neighboring cells they captured with nodes and connecting the parent nodes with their child nodes. To reduce the computational tasks, two kinds of pruning conditions are given here. **a** Pre-pruning. If multiple nodes in the same level are related the same cell (cell 22), only the node with the smallest capture time (t_{cap} = 0.5 ms) is allowed to have child nodes. **b** Post-pruning. If a node has a capture time (t_{cap} = 1.3 ms) smaller than a node (t_{cap} = 1.5 ms) in a older level and they have the same cell index (cell 23), then the node in the older level is invalid and its child nodes are removed. **c** Schematic capture conditions at time t = 0.8 ms and t = 1.5 ms, corresponding to the conditions shown in a and b, respectively.

2.8. Overall algorithm

The overall algorithm for the current CA solidification model is given in Algorithm 1. First, the initial microstructure of the base plate and powder layers is generated as a random microstructure with randomly oriented grains and saved to the hard disk. A number of layers are loaded into the memory. The scanning pattern is also calculated based on the processing conditions. Then, the simulation proceeds pass by pass. For each scanning pass, the maximum temperature of each CA cell in the memory is calculated. If its maximum temperature is larger than the liquidus temperature, it will be set to liquid. The time t_{uc} when each liquid cell becomes undercooled is also calculated to track the undercooled region. Then, solidification is simulated with a constant time step Δt. The data of interface cells and the indices of undercooled cells are saved in two containers. In each time step, new undercooled cells and new interface cells are added into the container for undercooled cells and the container for interface cells, respectively. The temperature of the undercooled cells are updated. Then, the program updates the growth length and performs capture checks for each interface cell with the decentered growth algorithm and the multi-level capture algorithm. Newly transformed interface cells will be added into the container for interface cells. The interface cells which do not have liquid neighbors are transformed into solid cells and are removed from the container for interface cells and the container for undercooled cells.

Algorithm 1: The overall algorithm for the CA solidification model.

```
Initialize the microstructure with a random Voronoi tessellation;
Calculate the scanning pattern for all the layers;
t ← 0 ;
Δt ← ξ Δx / v_s ;
foreach scanning pass do
    Calculate the maximum temperature for each cell;
    Set the cells with their maximum temperature above the
      liquidus temperature T_l to liquid;
    Calculate the time t_uc when each liquid cell become
      undercooled;
    while t < t_end,pass do
        Add new undercooled cells and new interface cells;
        Calculate temperature for each undercooled cell;
        Update growth length for each interface cell;
        Perform capture check with the multi-level capture
          algorithm;
        Add new interface cells;
        Remove interface cells which transform into solid from
          the container for interface cells and the container for
          undercooled cells;
        t = t + Δt;
    Check if deposit a new layer in the simulation domain;
```

2.9. Experiments

Commercial NiTi powder (TLS Technik GmbH, Bitterfeld, Germany) was used to fabricate the three NiTi parts by laser powder bed fusion

(L-PBF) under argon protection. L-PBF was performed on an Aconity3D Midi (Aconity3D GmbH, Germany) machine equipped with a laser source featuring a maximum power of 1000 W and a beam with a Gaussian power distribution. The L-PBF processing parameters are summarized in the Supplementary Table 2. Crystallographic textures were investigated using electron back-scatter diffraction (EBSD) technique. The measurements were performed by the Helios G4 SEM microscope equipped with EDAX EBSD detector under 25 kV accelerating voltage and 25 nA beam current. MTEX [37] is employed to generate pole figures based on EBSD measurements and simulated microstructures.

3. Results

3.1. Influence of the time step size

To verify the independency of the proposed model on the time step size, different time steps (ξ = 0.04, 0.5, 1.0, 1.5, 2.0) have been employed to simulate a directional solidification case. The simulation is performed in a $400\times400\times400\,\mu m^3$ domain with a cell size of 1.0 μm. The initial microstructure is generated with a Voronoi tessellation, while no nucleation is employed during the simulation. A temperature gradient of 1.0×10^6 K/m is applied in the Z direction. As the simulation domain cools at a rate of 5.0×10^5 K/s, directional solidification occurs. The fully solidified microstructure in the two simulations with ξ = 0.04 and ξ = 2.0 are given in Fig. 2. The microstructures in the plane-YZ (Figs. 2b and 2c) and plane-XY (Figs. 2e and 2f) in the simulations with ξ = 0.04 and ξ = 2.0 are similar to each other. Moreover, both the two simulations exhibit a ⟨100⟩ fiber texture, as shown in Figs. 2h and 2i. However, some minor differences (highlighted with circles) can be observed in the center of Figs. 2b and 2c. These subtle differences are caused by rounding errors and conditions that two interface cells may capture the same liquid cell at exactly the same time, which is rare but possible to occur. In Fig. 2d, the evolution of the volume fractions of three three arbitrarily chosen grains are plotted against the Z coordinate for the two simulations with ξ = 0.04 and ξ = 2.0. Due to different local growth competition conditions, the volume fractions of grain-1 and grain-3 increases continuously, while the volume fraction of grain-2 initially increases and then decreases. The volume fraction curves from the two simulations overlap, indicating that the value of ξ has little influence. In conclusion, the dependence of CA growth on time step size has been successfully eliminated. The performance of simulations with different ξ values are presented in Fig. 2d. With increasing ξ, the time step size increases and the number of time steps to finish the simulation decreases, leading to a decrease in the computational time. However, with increasing time step size, the number of captured interface cells increases, which increases the computational cost for each time step. In this case, the total computation time first decreases and then increases with increasing ξ. The minimum computation time is obtained with ξ around 1.0 for the directional solidification case.

3.2. Model validation with a 316L steel sample

The current model is validated by simulating the microstructure of a 316L component with a {110}⟨001⟩ Goss texture, which was reported in the work of Andreau et al. [38]. The simulation is performed in a $2000\times2000\times4500\,\mu m^3$ domain with a cell size of 5 μm. The initial microstructure is generated with a Voronoi tessellation. In the simulation, the scanning direction (SD) is parallel or anti-parallel with the X+ direction, while the building direction (BD) is in the Z+ direction. The simulation results are given in Fig. 3. The color is determined as the inverse pole figure (IPF) color in the Z+ direction. For a better illustration, two slices are made in the plane-XY and plane-YZ which are perpendicular to the Z axis and the X axis, respectively. The simulated microstructure in the upper part ($2500\,\mu m \le z \le 4500\,\mu m$) of plane-YZ (BD-TD) (Fig. 3b) agrees with the bulk microstructure (Fig. 3c) from the experiments. The green grains, namely ⟨110⟩ ∥ Z grains, dominate in the boundary of the melt pool as a result of the orientation selection effect of the neighboring laser passes. In the center of the melt pool, the temperature gradient is parallel with the Z axis, leading to the formation of red grains, namely ⟨100⟩ ∥ Z grains, which propagate along the Z axis. The ⟨100⟩ ∥ Z grains in the experiment show some waviness due to the oscillations in the melt pool. As the simulation does not consider melt pool oscillations, such a waviness is not observed in Fig. 3b. In the lower part ($0\,\mu m \le z \le 2000\,\mu m$) of plane-YZ, a transition from a random microstructure to a microstructure dominated by ⟨100⟩ ∥ Z grains is observed, as shown in Fig. 3d. The short transition region indicates a high selection rate on dominant orientations. The selection rate is influenced by many factors including melt pool shape, cell size and heat accumulation. Here, the width and height of the simulated melt pool deviate from the mean width and height of the experimental melt pool by 5 μm, which is acceptable within the margin of error, as shown in Fig. 3f. Note the high selection rate is related to the deviation in the melt pool dimensions. A smaller selection rate is observed, when the simulation is performed with a melt pool which matches the mean dimensions of the experimental melt pool. The details can be found in the Supplementary Material (Supplementary Section 4). The pole figure shown in Fig. 3g is generated based on the microstructure in Fig. 3e. The simulated pole figure matches the experimental pole figure (Fig. 3h), which is close to the {110}⟨001⟩ Goss texture.

The current CA model has been benchmarked against models reported in the literature [17,23] by simulating the microstructure of a 316L sample using similar computational resources, as shown in Table 1. Compared to a CA model [23] implemented with a shared memory, our CA model is approximately 20 times faster (12 core hours versus 220 core hours). When compared to a CA model utilizing a distributed memory [17], our model demonstrates an improvement in speed by nearly two orders of magnitude (32 core hours versus 9360 core hours). Note the comparison here remains qualitative, as numerous external factors may influence the computational performance of CA models. This acceleration comes from two sources. First, a larger time step (ξ = 1.0) is employed in the current CA model, which is safely achieved by analytically calculating the growth length and employing a multi-level capture algorithm. Secondly, a pass-by-pass sparse temperature algorithm is implemented in the current model, which reduces the computational tasks for melting and limits the temperature calculation in the undercooled region. When the simulation is performed with a small time step (ξ = 0.04) and without the pass-by-pass sparse temperature algorithm (referred as Base in Table 1), it takes approximately 360 h using 64 cores of two AMD EPYC 7452 CPUs, which is two orders of magnitude slower.

3.3. Model validation with NiTi samples

The current model is further validated by simulating the microstructure of additively manufactured NiTi samples (sample-A, sample-B and sample-C, corresponding to low, medium and high laser powers, respectively). The process parameters can be found in the Supplementary Table 2. To avoid cracking, the scanning direction is rotated by 67 degrees when depositing a new layer. Different process conditions lead to different melt pool shapes and thus different microstructures. The experimental melt pool shapes in top layers of manufactured samples are employed to calibrate our modified thermal model, which enables a good fitting of melt pools in the conduction mode or the transition mode. To accounting for the accumulated heat from previously deposited layers, an initial temperature of 523 K is employed in the thermal model. Material parameters including density, thermal conductivity and the specific heat are constant for all the simulations, which are given in Supplementary Table 1. In both the simulations and the experiments, a coordinate system is defined based on the building direction and the sample geometry. The Z axis is parallel with the build direction, while the X and Y axes are perpendicular to the building direction. Note the X axis does not represent the scanning

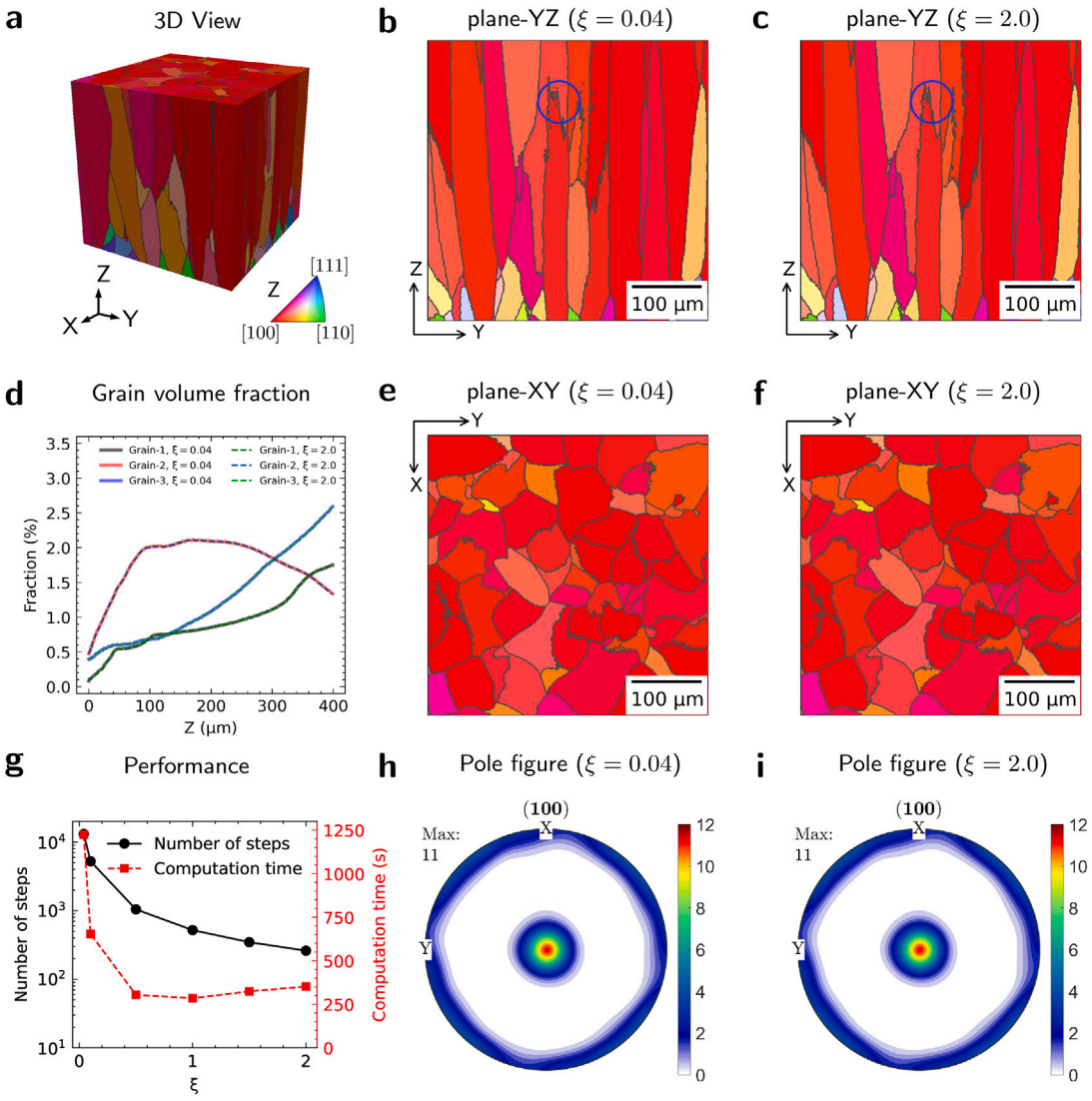

Fig. 2. Validation of time step independence with a directional solidification case. The temperature gradient is applied in the positive Z direction. The simulation domain size is $400 \times 400 \times 400\,\mu m^3$. IPF (inverse pole figure) color with respect to Z axis is employed. **a** 3D view. **b**, **c** Plane-YZ ($x = 200\,\mu m$) in the simulations with $\xi = 0.04$ and $\xi = 2.0$. **d** Evolution of volume factions of three grains with respect to the Z coordinate in the simulations with $\xi = 0.04$ and $\xi = 2.0$. ξ value has little influence on the grain volume fraction evolution. **e**, **f** Plane-XY ($z = 400\,\mu m$) in the simulations with $\xi = 0.04$ and $\xi = 2.0$. **g** Optimal computation time is obtained with $\xi = 1.0$. **h**, **i** Pole figure in the simulations with $\xi = 0.04$ and $\xi = 2.0$ (generated based on e and f, respectively). (For interpretation of the references to color in this figure legend, the reader is referred to the web version of this article.)

Table 1
Comparison between the current CA model with CA models reported in literature [17,23] in case of simulating microstructure of a 316L steel sample.

Model	Domain size (μm^3)	Cell size (μm)	CPU type	Frequency	Cores	Time (h)	Core hours
Current	$2000 \times 2000 \times 4500$	5.0	AMD EPYC 7452	2.35 GHz	8	2.2	17.6
Current	$2000 \times 2000 \times 4500$	5.0	AMD EPYC 7452	2.35 GHz	16	1.5	24.0
Current	$2000 \times 2000 \times 4500$	5.0	AMD EPYC 7452	2.35 GHz	32	1.2	38.4
Current	$2000 \times 2000 \times 4500$	5.0	AMD EPYC 7452	2.35 GHz	64	1.0	64.0
Current	$2000 \times 2000 \times 4500$	5.0	Intel Xeon E5-6248R	3.00 GHz	8	1.5	**12**
Model [23]	$2055 \times 2055 \times 4750$	5.0	AMD Ryzen 7 1700X	3.40 GHz	8	27.5 [23]	**220**
Base	$2000 \times 2000 \times 4500$	5.0	Intel Xeon E5-6248R	3.00 GHz	64	360	**12 960**
Current	$750 \times 750 \times 562.5$	1.875	AMD EPYC 7452	2.35 GHz	64	0.5	**32**
Model [17]	$750 \times 750 \times 562.5$	1.875	Intel Xeon Platinum 8168	2.70 GHz	144	65 [17]	**9360**

direction, as the scanning direction rotates by 67 degrees for each new layer. Experimental bulk microstructures are measured with EBSD in the plane-XY and the plane-YZ of the additively manufactured samples. For comparison, slices are made from the simulated three-dimensional microstructure in the plane-XY and plane-YZ. The cell size is determined as an appropriate value (1.0 μm) to balance the requirement of selection rate and computational cost. A sufficiently large domain ($800 \times 800 \times 3000\,\mu m^3$) is employed to capture the microstructure evolution from a random microstructure to a steady-state microstructure, corresponding to the experimental bulk microstructure. The random microstructures in the substrate and powder layers are generated with a Voronoi tessellation with an initial grain size of 15 μm. In all the NiTi simulations, a nucleation density of $2.0 \times 10^{14}\ m^{-3}$ is employed, which is determined by fitting the steady-state microstructure against the bulk

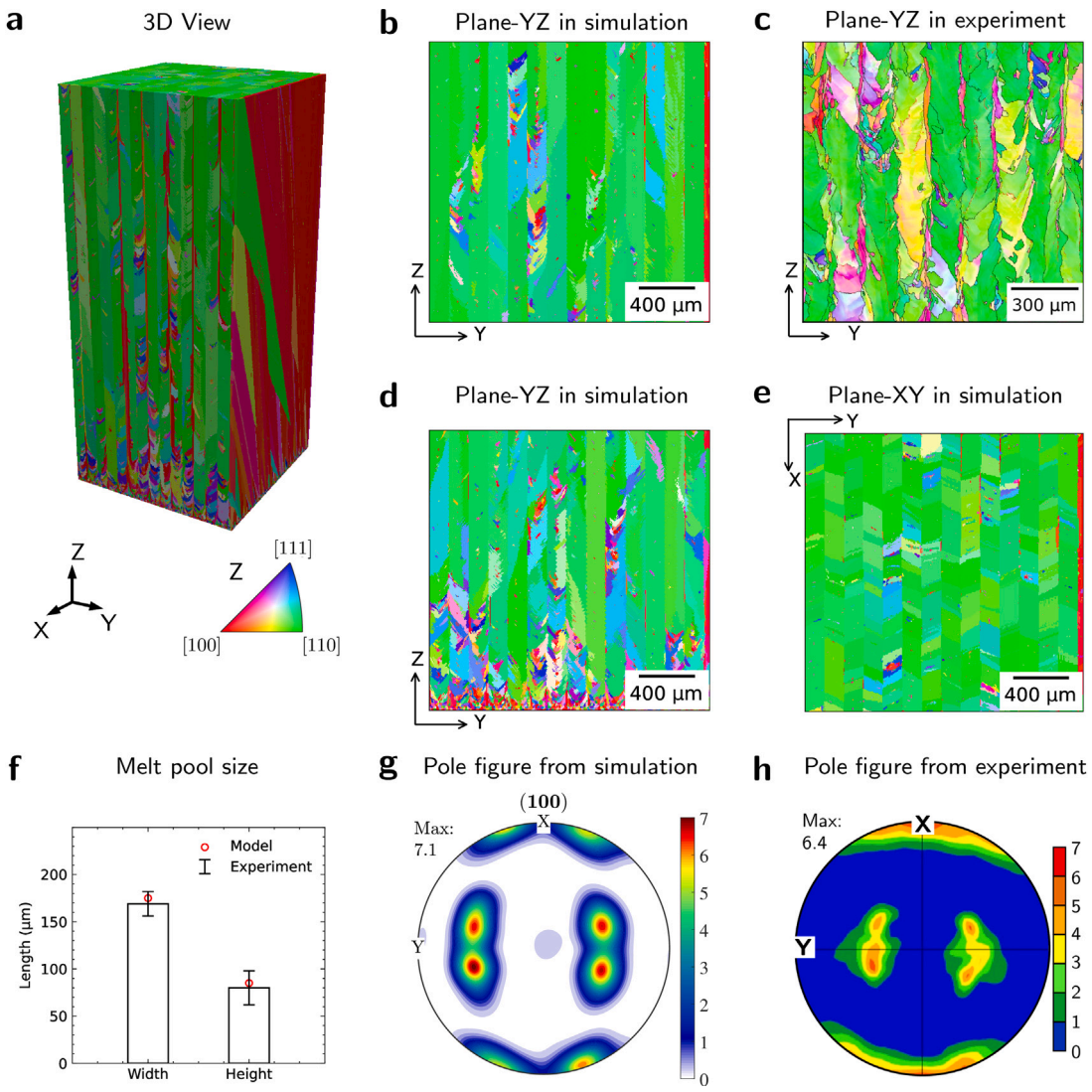

Fig. 3. Results from the simulations and the experiments for the 316L sample. The simulation domain size is $2000\times2000\times4500\,\mu m^3$. **a** 3D view. **b**, **d** Simulated microstructure in the upper part ($2500\,\mu m \le z \le 4500\,\mu m$) and the lower part ($0\,\mu m \le z \le 2000\,\mu m$) of plane-YZ ($x = 1000\,\mu m$). **c** Experimental microstructure in plane-YZ. In both the simulation and the experiment, $\langle 110\rangle \parallel Z$ (green) grains dominate the microstructure and stripe-like $\langle 100\rangle \parallel Z$ (red) grains propagate along the building direction (Z). **e** Simulated microstructure in the plane-XY ($z = 4500\,\mu m$). **a**-**e** are colored with IPF (inverse pole figure) color with respect to the Z axis. **f** Melt pool dimensions in the experiments and simulations. **g** Simulated pole figure (generated based on e). **h** Experimental pole figure. A $\{110\}\langle 001\rangle$ Goss texture is identified in both the simulation and the experiment. Figures 2c, 2f and 2 h are adapted from Andreau et al. [38]. (For interpretation of the references to color in this figure legend, the reader is referred to the web version of this article.)

microstructure (see Section 4.1). At the beginning of the simulations, three or four layers are deposited to make sure the bottom of the melt pool does not go beyond the simulation domain. In the end of the simulations, to ensure that simulated microstructures in top layers represent bulk microstructures, the laser scanning process is extended beyond the simulated domains until no re-melting occurs within these specified domains.

For NiTi sample-A, the thermal model is calibrated with the average experimental melt pool shape from top layers. The simulated melt pool is compared with an experimental melt pool in Fig. 4f, where a good agreement is achieved. The steady-state microstructure in the upper part ($2200 \le z \le 3000\,\mu m$) of the simulation domain is compared with the experimental bulk microstructure, as shown in 4. In plane-YZ, semi-elliptical shapes are observed in both the simulation and the experiments, as shown in Figs. 4b and 4c, respectively. The semi-elliptical shapes may consist of a large grain or several small grains with different orientations. The grains in the semi-elliptical shapes have orientations which are favorable to grow locally. Those grains propagate along the build direction for a few layers until their orientations are not favorable due to the rotation of the scanning direction between adjacent layers. In the plane-XY of the simulation (Fig. 4d), the microstructure is characterized by rounded polygons consisting of several grains, where the edges of the polygon are shaped with small columnar grains. The polygons are shaped by scanning passes from several layers. After scanning passes from one layer, columnar grains are formed with their edges parallel or inclined to the temperature gradient. The temperature gradient rotates as the scanning direction rotates between adjacent layers, leading to formation of polygonal shapes. The feature of large polygons can also be found in the plane-XY of the experiment, as shown in Fig. 4e. Note the experimentally measured plane-XY (Fig. 4e) may include several deposition layers due to experimental limitations, which might be the reason why some densely stacked columnar grains are observed in Fig. 4e. Besides, the experimental melt pools may oscillate during manufacturing, leading to differences in the locally favorable orientations. Pole figures shown in Figs. 4g and 4h are generated based on the microstructures in Figs. 4d and 4e for the simulation and the experiment, respectively. In the simulated pole figure shown in Fig. 4g, multiple local maximum points are observed, while the maximum points in the experimental pole figure (Fig. 4h) are more randomly distributed. This mismatch might be

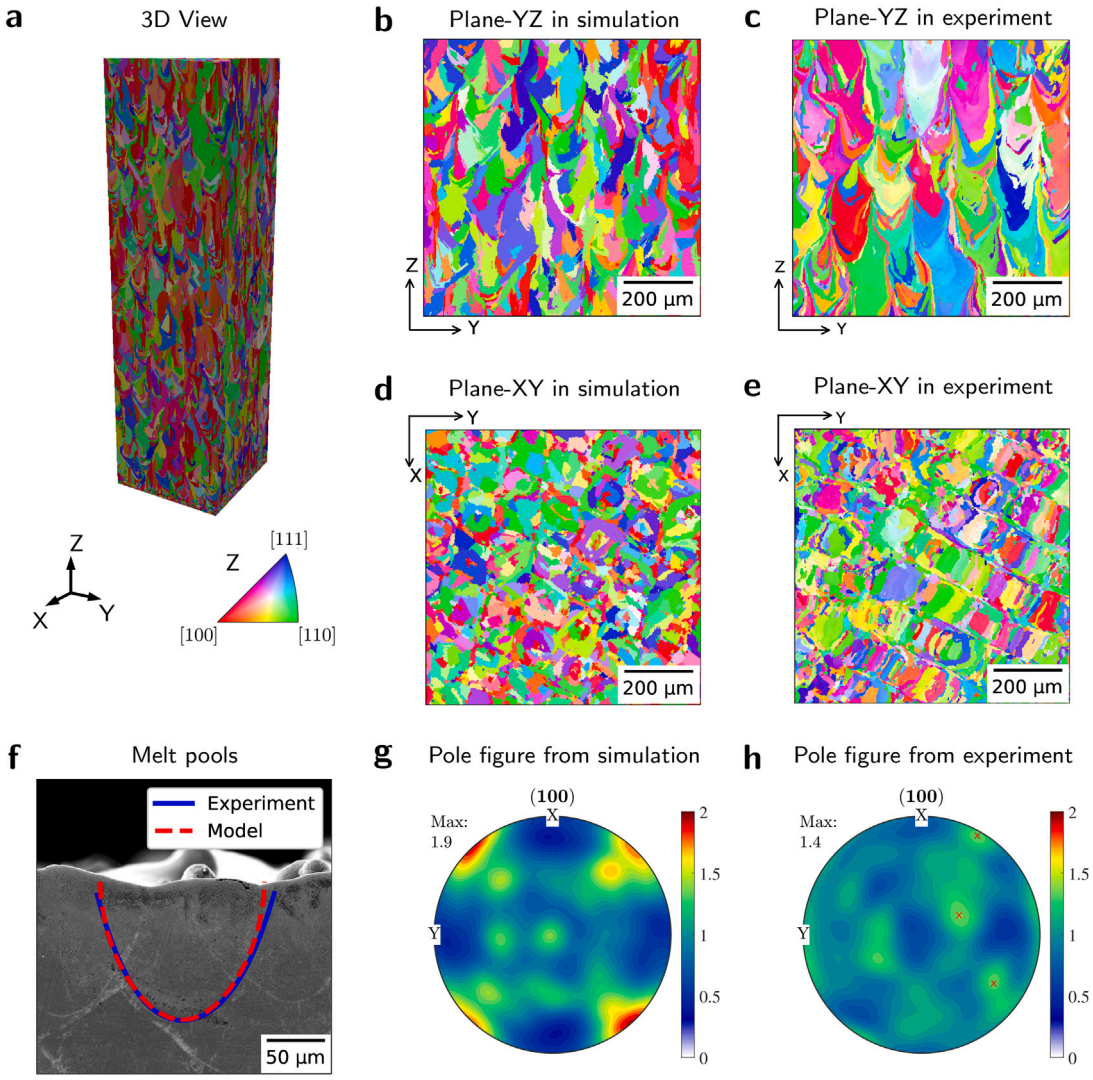

Fig. 4. Results from the simulation and the experiments for NiTi sample-A. The simulation domain size is $800 \times 800 \times 3000\,\mu m^3$. **a** 3D view. **b** Simulated microstructure in the upper part ($2200\,\mu m \leq z \leq 3000\,\mu m$) of plane-YZ ($x = 400\,\mu m$). **c** Experimental microstructure in plane-YZ. In plane-YZ, semi-elliptical shapes consisting one large grain or several small grains with different orientations are observed in both the simulation and the experiment. **d** Simulated microstructure in plane-XY ($z = 3000\,\mu m$). **e** Experimental microstructure in plane-XY. In plane-XY, polygons consisting of several small grains are observed in both the simulation and the experiment. **a**-**e** are colored with IPF (inverse pole figure) color with respect to Z axis. **f** The modeled melt pool shape fits the experimental melt shape in the cross section. **g**,**h** Simulated and experimental pole figure (generated based on d and e, respectively). A weak texture is observed in both f and g. (For interpretation of the references to color in this figure legend, the reader is referred to the web version of this article.)

caused by the experimental limitations and the oscillation of the melt pool during manufacturing. The maximum intensity in the simulation is around 1.9, indicating that sample-A has a very weak texture. This value is also close to the maximum intensity (1.4) in the experiment pole figure. In this case, the simulation is in acceptable agreement with the experimental results.

Different from the conduction-mode melt pool in NiTi sample-A, the melt pool in NiTi sample-B is in transition mode. The lower part of the transition-mode melt pool, which will not be remelted by subsequent laser passes, is well fitted with the thermal model, as shown in Fig. 5f. The simulated microstructure, as well as the experimental microstructure, is presented in Fig. 5 for comparison. Unlike sample-A, the microstructure of sample-B is dominated by ⟨100⟩ ∥ Z (red) grains, with one of their ⟨100⟩ crystallographic directions parallel with the Z axis. This indicates that ⟨100⟩ ∥ Z orientations are globally favorable. In the plane-YZ in the simulation, as shown in Fig. 5b, some stripe-like grains with globally unfavorable orientations[1] like ⟨210⟩ ∥ Z (yellow), ⟨211⟩ ∥ Z (purple) and ⟨110⟩ ∥ Z (green) propagate along the build direction (Z axis) in the ⟨100⟩ ∥ Z grain matrix, extending over a few layers. Similarly, stripe-like grains with globally unfavorable orientations can be identified in the plane-YZ of the experiment, as shown in Fig. 5c. Due to the oscillations of the melt pool, those grains with globally unfavorable orientations in the experiment exhibit some waviness. This is not observed in the simulation, as the simulation employed a stable melt pool without oscillations. In the plane-XY in the simulation (Fig. 5d), small grains with globally unfavorable orientations[1] like ⟨210⟩ ∥ Z (yellow), ⟨211⟩ ∥ Z (purple), ⟨110⟩ ∥ Z (green) and ⟨111⟩ ∥ Z (blue) are randomly located in the ⟨100⟩ ∥ Z grain matrix, which agrees with the experimental microstructure shown in Fig. 5e. The shape of the small grains with globally unfavorable orientations in the simulation is less smooth compared to the small grains in the

[1] The Miller indices shown here are estimations of real orientations.

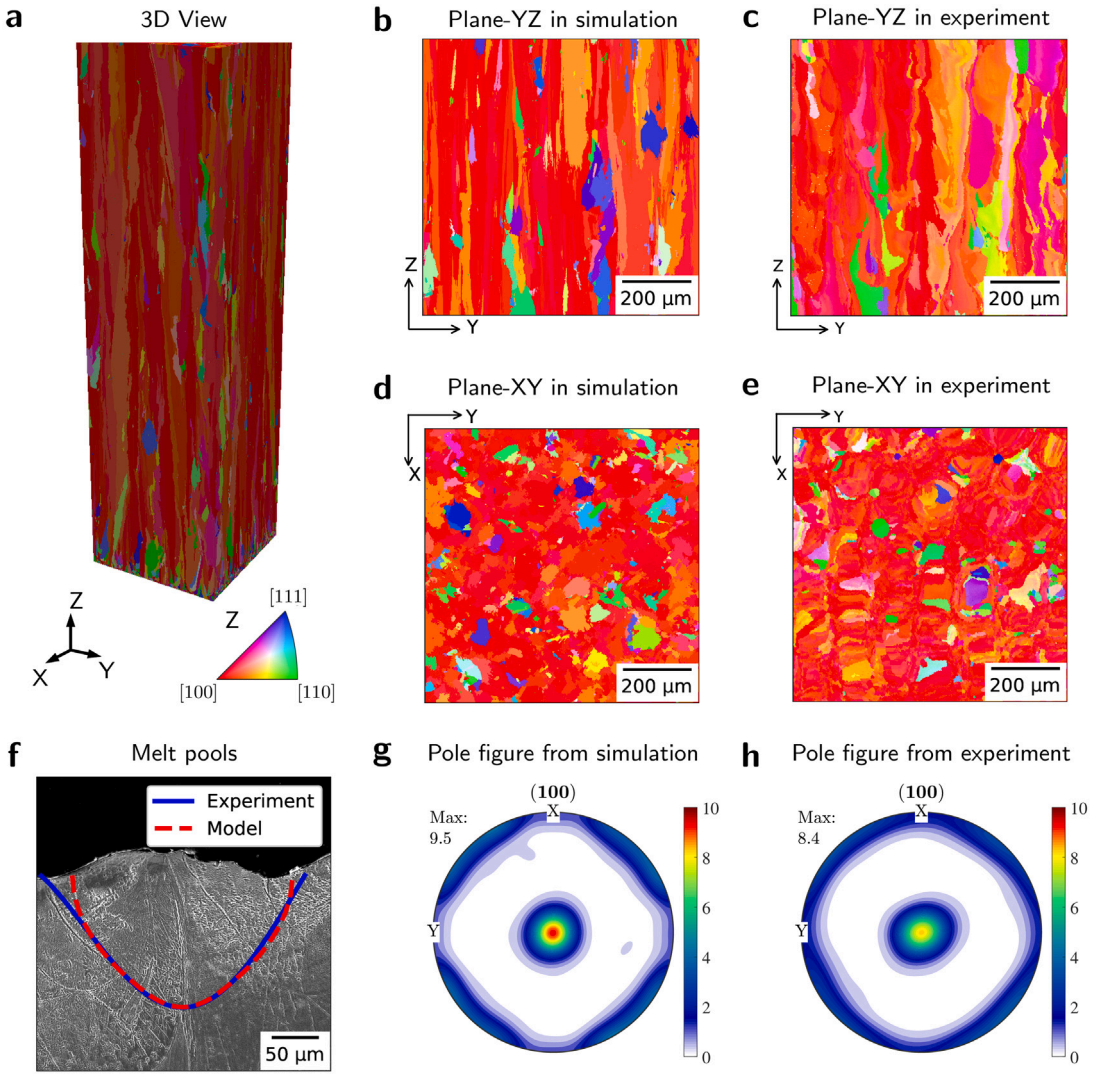

Fig. 5. Results from the simulation and the experiments for NiTi sample-B. The simulation domain size is $800 \times 800 \times 3000\,\mu m^3$. **a** 3D view. **b** Simulated microstructure in the upper part ($2200\,\mu m \leq z \leq 3000\,\mu m$) of plane-YZ ($x = 560\,\mu m$). **c** Experimental microstructure in plane-YZ. In plane-YZ, $\langle 100 \rangle \parallel Z$ (red) grains dominate the microstructure and stripe-like grains with globally unfavorable orientations like $\langle 210 \rangle \parallel Z$ (yellow), $\langle 211 \rangle \parallel Z$ (purple) and $\langle 110 \rangle \parallel Z$ (green) propagate along the building direction (Z axis). **d** Simulated microstructure in plane-XY ($z = 3000\,\mu m$). **e** Experimental microstructure in plane-XY. In plane-XY, small grains with globally unfavorable orientations like $\langle 210 \rangle \parallel Z$ (yellow), $\langle 211 \rangle \parallel Z$ (purple), $\langle 110 \rangle \parallel Z$ (green) and $\langle 111 \rangle \parallel Z$ (blue) are randomly located in the $\langle 100 \rangle \parallel Z$ grain matrix. **a**-**e** are colored with IPF (inverse pole figure) color with respect to Z axis. **f** The modeled melt pool shape fits the experimental melt shape in the cross section. **g**, **h** Simulated and experimental pole figure (generated based on d and e, respectively). A strong $\langle 100 \rangle$ texture is observed in both the simulation and the experiment. (For interpretation of the references to color in this figure legend, the reader is referred to the web version of this article.)

experiment; this is because interface curvature and grain growth are not considered in the growth algorithm of the CA simulation. In both the simulation and the experiment, the microstructure is dominated by $\langle 100 \rangle \parallel Z$ grains, which have one of their $\langle 100 \rangle$ crystallographic directions parallel with the Z axis and the other two $\langle 100 \rangle$ crystallographic directions oriented randomly. This leads to a strong $\langle 100 \rangle$ fiber texture in both the simulation and the experiment, as shown in 5g and 5h, which are generated based on the microstructure in 5d and 5e, respectively. The maximum texture intensity (9.5) in the simulation is close to that (8.4) in the experiment.

For NiTi sample-C (high laser power), the analytical thermal model is well fitted with the experimental melt pool shape, as shown in Fig. 6f. Similar to the microstructure of NiTi sample-B, $\langle 100 \rangle \parallel Z$ grains dominate the microstructure in the simulation and the experiment. In plane-YZ of the simulation, as shown in 6b, $\langle 100 \rangle \parallel Z$ (red) grains which propagate along the building direction dominate the microstructure, which agrees with the experimental observations in 6c. Due to nucleation, some extremely small grains (several cells) with unfavorable orientations exist in the $\langle 100 \rangle \parallel Z$ grain matrix in the simulation. However, due to the selection effect of the temperature gradient, the size of those grains are very small and they have little influence on the final texture. In the plane-XY of the simulation (Fig. 6d), the microstructure is composed of red $\langle 100 \rangle \parallel Z$ and near-red columnar grains. This agrees with the experimental result in Fig. 6e. The pole figure of the simulation shown in Fig. 6g is generated based on the microstructure in Fig. 6d, while the pole figure of the experiment shown in Fig. 6h is generated based on an XRD (X-ray diffraction) measurement. The reason for not considering microstructure in Fig. 6e is that the resultant pole figure is not representative due to insufficient number of grains in the EBSD dataset (see Section 5 in Supplementary Material). The simulated pole figure agrees well with the pole figure based on the XRD measurement.

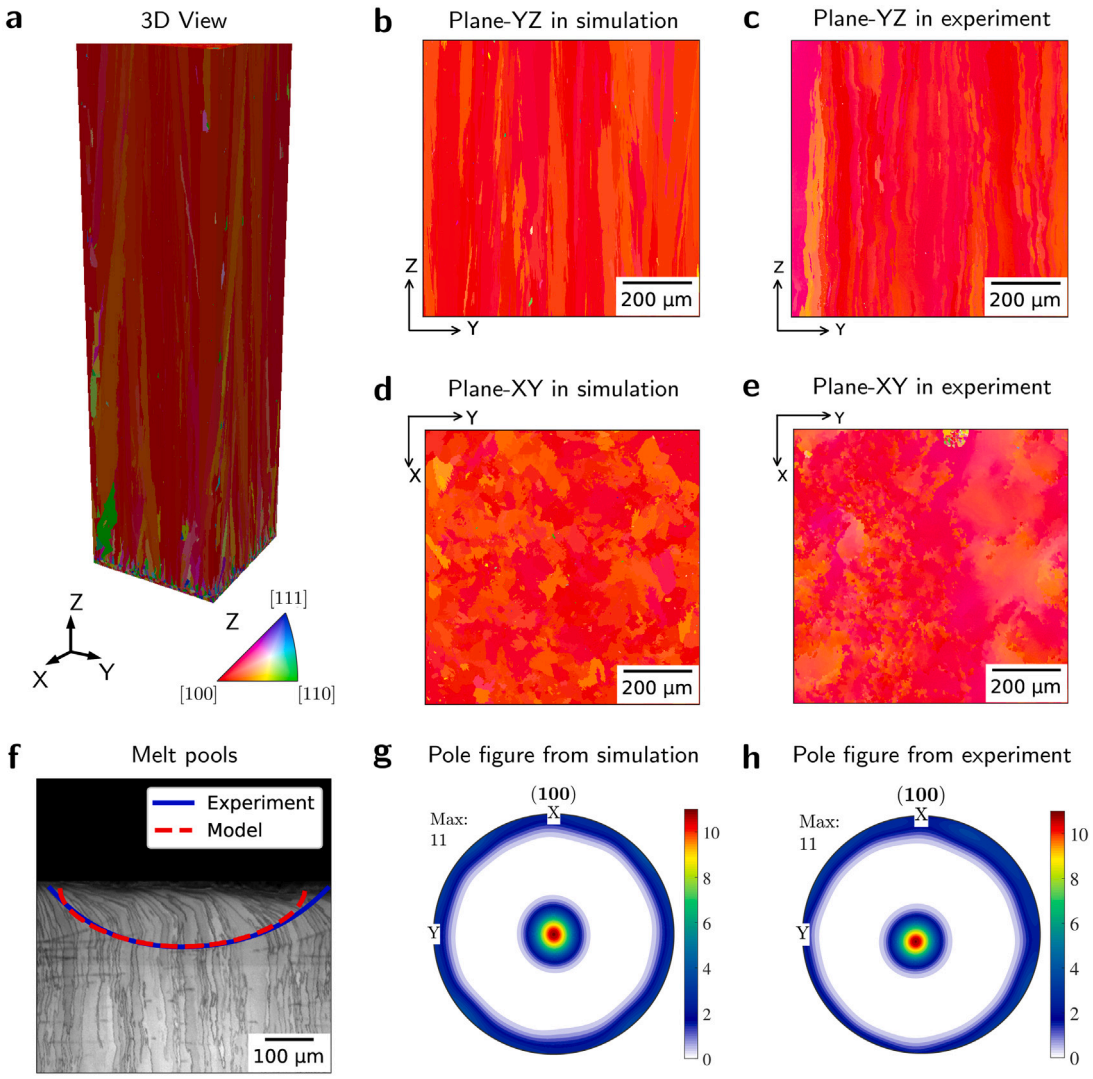

Fig. 6. Results from the simulation and the experiments for NiTi sample-C. The simulation domain size is $800 \times 800 \times 3000\,\mu m^3$. **a** 3D view. **b** Simulated microstructure in the upper part ($2200\,\mu m \le z \le 3000\,\mu m$) of plane-YZ ($x = 400\,\mu m$). **c** Experimental microstructure in plane-YZ. In plane-YZ, $\langle 100 \rangle \parallel$ Z grains dominate the microstructure, which propagate along the building direction (Z axis). **d** Simulated microstructure in plane-XY ($z = 3000\,\mu m$). **e** Experimental microstructure in plane-XY. In plane-XY, the microstructure is mainly $\langle 100 \rangle \parallel$ Z grains with unstructured shapes. **a-e** are colored with IPF (inverse pole figure) color with respect to the Z axis. **f** The modeled melt pool shape fits the experimental melt shape in the cross section. **g**, **h** Simulated and experimental pole figure (generated based on d and e, respectively). Both the simulated and the experimental pole figures show a strong $\langle 100 \rangle$ texture. (For interpretation of the references to color in this figure legend, the reader is referred to the web version of this article.)

4. Discussion

4.1. Simulation of steady-state bulk microstructure

The intention of the current work is to validate the developed CA model by comparing simulated bulk microstructures with experimental ones under different processing conditions. In AM, when enough layers have been deposited, the deposited microstructure reaches a steady state condition. The steady-state microstructure is obtained as a balance between an orientation selection effect and nucleation. With increasing height, grains with unfavorable orientations gradually disappear due to orientation selection of temperature gradients, while nucleation introduces new grains with different orientations. The balance between orientation selection and nucleation will be illustrated with NiTi sample-B.

The simulation of NiTi sample-B was performed with a domain of $800 \times 800 \times 3000\,\mu m^3$ and a cell size of $1.0\,\mu m$. The microstructure in plane-XY at different heights are given in Fig. 7. The simulation starts from a random microstructure, as show in Fig. 7a. With increasing height, temperature gradients from different laser passes select grains with favorable orientations ($\langle 100 \rangle \parallel$ Z grains, namely, red grains), and the fraction of non-red grains decreases, until a steady-state microstructure is reached at a height around $1800\,\mu m$. As shown in Figs. 7d, 7e and 7f, the microstructures at $1800\,\mu m$, $2400\,\mu m$ and $3000\,\mu m$ are similar, where small non-red grains are located randomly in the matrix of $\langle 100 \rangle \parallel$ Z (red) grains. The fraction of red grains as a function of height (Z) is given in Fig. 7g. Here, red grains are defined as grains with $\theta < 20°$, where θ is the minimum angle between the $\langle 100 \rangle$ crystallographic directions and Z+ direction. With increasing height, the fraction of red grains increases until a plateau is reached at a height of around $1800\,\mu m$. The fluctuation observed in Fig. 7g is caused by nucleation. The existence of a plateau confirms the steady-state condition.

The steady-state microstructure is achieved as a balance between orientation selection and nucleation. The fraction of $\langle 100 \rangle \parallel$ Z (red) grains in the steady-state microstructure is influenced by the nucleation density n_n. To illustrate this effect, simulations of NiTi sample-B have been performed with three different nucleation densities n_n: $2 \times 10^{13}\,m^{-3}$ (NS1), $2 \times 10^{14}\,m^{-3}$ (NS2) and $2 \times 10^{15}\,m^{-3}$ (NS3). The simulated steady-state microstructures are presented in Fig. 8. In NiTi sample-B, $\langle 100 \rangle \parallel$ Z (red) orientations are globally favorable, while other orientations (non-red) are only locally favorable in certain regions, referred to as LF

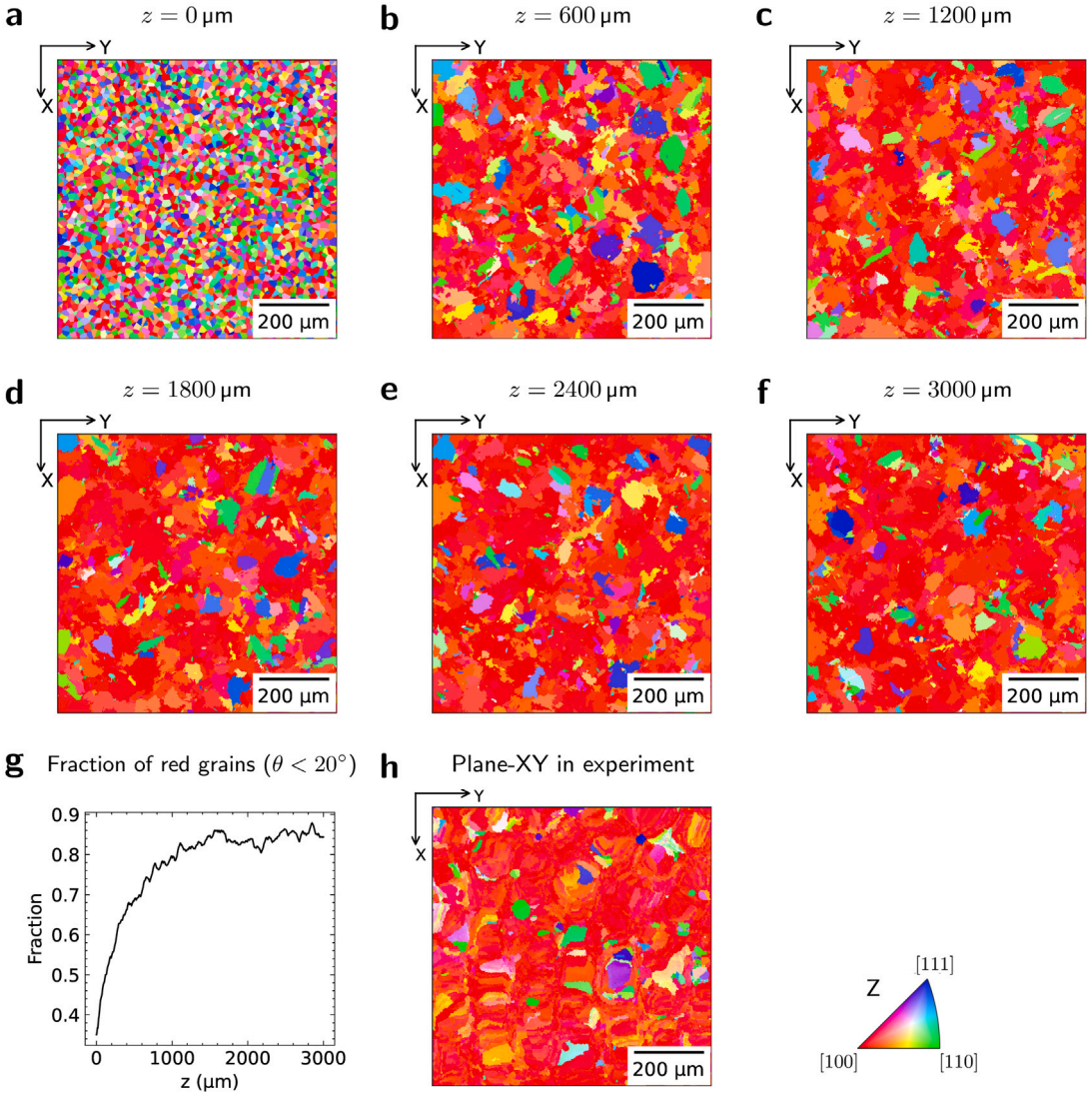

Fig. 7. A steady-state microstructure is obtained after depositing enough layers in NiTi sample-B. a, b, c, d, e, f Microstructure in plane-XY at different heights (0 μm, 600 μm, 1200 μm, 1800 μm, 2400 μm and 3000 μm). **g** The fraction of red grains increases with increasing height. Red grains are defined as grains with $\theta < 20°$, where θ is the minimum angle between the ⟨100⟩ crystallographic directions and Z+ direction. **h** Experimental microstructure in plane-XY. (For interpretation of the references to color in this figure legend, the reader is referred to the web version of this article.)

(locally favorable) regions. LF regions scatter in the simulation domain and are disconnected. Whether LF regions are occupied by ⟨100⟩ ∥ Z (red) grains or grains with LF orientations depends on the nucleation density. At a lower nucleation density ($n_n = 2{\times}10^{13}$ m^{-3}), LF regions are more likely to be filled by ⟨100⟩ ∥ Z grains, as shown in Figs. 8a and 8d. In contrast, at a higher nucleation density ($n_n = 2{\times}10^{15}$ m^{-3}), LF regions are predominantly occupied by LF-oriented grains, as seen in Figs. 8c and 8f. Consequently, the fraction of ⟨100⟩ ∥ Z (red) grains decreases with increasing nucleation density. Fig. 8g shows the fraction of ⟨100⟩ ∥ Z (red) grains as a function of height (Z) for simulations NS1, NS2, and NS3. The plateaus confirm that steady states are achieved in each case. As the nucleation density n_n increases from $2.0{\times}10^{13}$ m^3 to $2.0{\times}10^{15}$ m^3, the fraction of ⟨100⟩ ∥ Z (red) grains in the steady state decreases from 0.9 to 0.6. The maximum intensity of the ⟨100⟩ fiber texture decreases, as shown in Figs. 8h and 8i. In the experimental microstructure, the fraction of ⟨100⟩ ∥ Z (red) grains is around 0.86 and the maximum texture intensity is around 8.4, which closely match the steady-state microstructure of the simulation with $n_n = 2{\times}10^{14}$ m^{-3}. Therefore, this nucleation density value ($n_n = 2 \times 10^{14}$ m^{-3}) is used for all the NiTi simulations presented in this work. Notably, this nucleation density is close to that used in Teferra and Rowenhorst's work ($3{\times}10^{14}$ m^{-3}) [17].

4.2. Formation of grain morphology and texture

For a crystal with a cubic crystal symmetry, the preferential growth direction is always the ⟨100⟩ direction [39]. For solidification, the preferential orientation which dominates the growth has one of its ⟨100⟩ crystallographic directions parallel with the temperature gradient. In other words, the temperature gradient selects the preferential orientation, resulting in different microstructures. In this part, we will examine the selection effect of the temperature gradient, analyzing how it influences the formation of the 110⟨001⟩ texture in the 316L steel sample, as well as the textures observed in the NiTi samples.

For multi-layer AM, the temperature gradient profile is complex, especially when the scanning direction is rotated between adjacent layers. To simplify the problem, we divided the temperature gradients in a single melt pool into two types: vertical temperature gradient (VTG) and inclined temperature gradient (ITG), as shown in Fig. 9a, which is the boundary of a melt pool in a cross section perpendicular to the scanning direction. This classification is only applied to the lower part of the melt pool, as the upper part of the melt pool will be remelted by laser passes in subsequent layers.

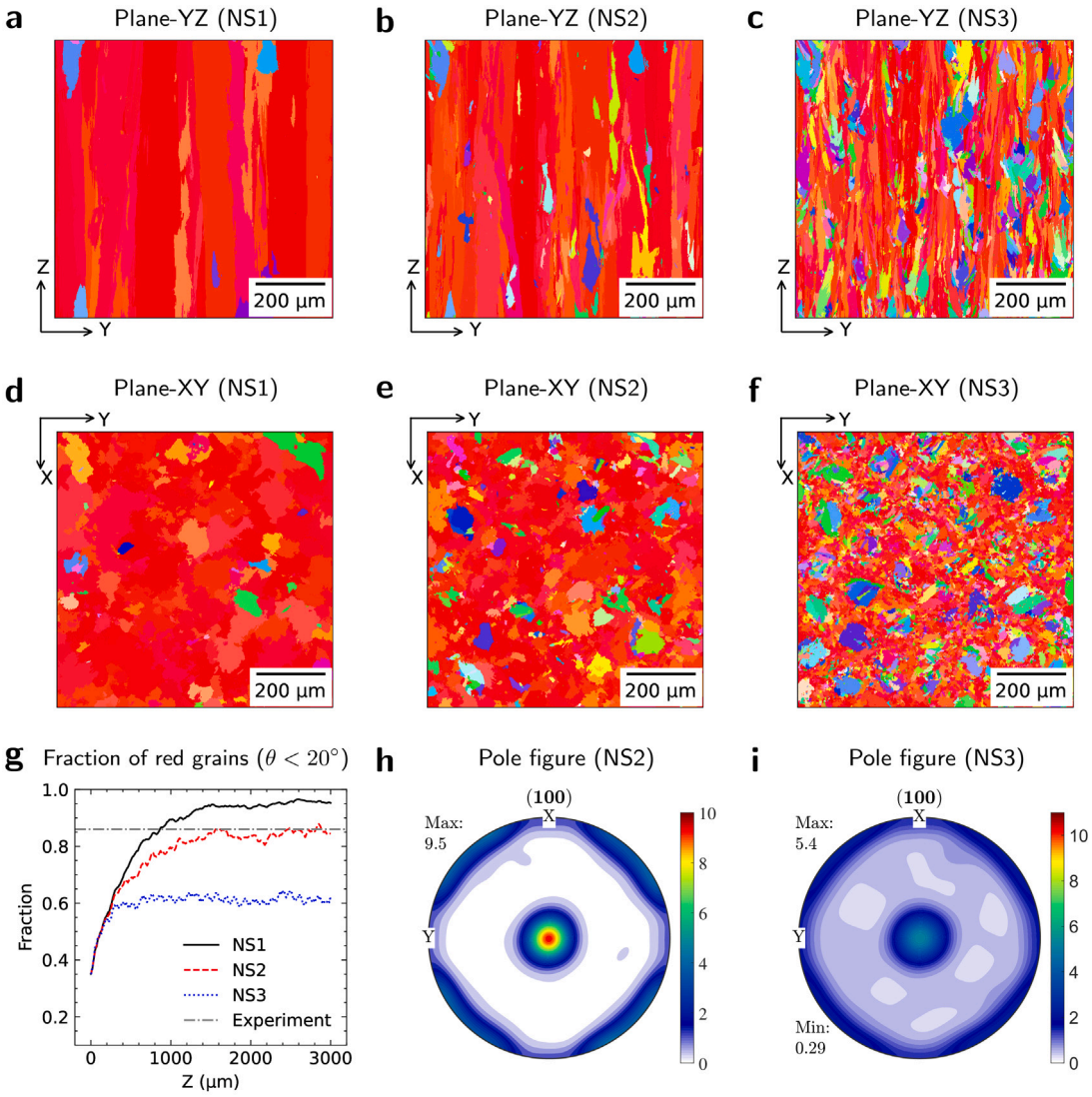

Fig. 8. Influence of the nucleation density on steady-state microstructure. Simulations of NiTi sample-B are performed for with different nucleation density n_n: 2×10^{13} m^{-3} (NS1), 2×10^{14} m^{-3} (NS2) and 2×10^{15} m^{-3} (NS3). The domain size is $800\times800\times3000$ μm^3. **a, b, c** Microstructure in the upper part of plane-YZ (2200 μm ≤ z ≤ 3000 μm at x = 400 μm) in simulations NS1, NS2 and NS3. **d, e, f** Steady-state microstructure (taken from plane-XY at z = 3000 μm) in simulations NS1, NS2 and NS3. IPF (inverse pole figure) colors with respect to the Z axis are employed in figures a–f. **g** The fraction of ⟨100⟩ ∥ Z (red) grains with respect to height (Z) in the simulations NS1, NS2 and NS3. With increasing nucleation density, the fraction of ⟨100⟩ ∥ Z (red) grains in the steady-state microstructure decreases. **h, i** Pole figures for simulations NS2 and NS3, generated based on the microstructures in e and f, respectively. (For interpretation of the references to color in this figure legend, the reader is referred to the web version of this article.)

The 316L steel sample is employed as an example to explain the formation of the {110}⟨001⟩ texture. The melt pool boundaries of laser passes from different layers are superimposed on the microstructure in a selected region in plane-YZ in the simulation, as shown in Fig. 9c. Here, the in-plane component of the temperature gradient can be assessed in the direction perpendicular to the melt pool trace line. In the center of the melt pool, VTG is parallel with the Z axis, which preferentially selects ⟨100⟩ ∥ Z (red) grains, that propagate along the building direction as thin stripes. In the junction region between two neighboring laser passes, ITGs are inclined at an angle of approximately 45 degrees with the Z-axis. Furthermore, ITGs from neighboring laser passes are nearly perpendicular to each other. This configuration uniquely determines a favorable {110}⟨001⟩ orientation, with two of its ⟨100⟩ crystallographic directions parallel with the ITGs. This leads to a {110}⟨001⟩ Goss texture. In real AM conditions, the temperature gradients are not perfectly aligned within the plane perpendicular to the scanning direction. The out-of-plane components of the temperature gradient introduce small deviations in the resulting 110⟨001⟩ Goss texture, as shown in Figs. 3g and 3h.

For NiTi samples, the scanning direction is rotated by 67 degrees when adding a new layer. In this case, the scanning direction of each layer is not necessarily perpendicular to the plane-YZ, leading to different melt pool boundaries in the YZ plane, as shown in Figs. 9c, 9e and 9f. Meanwhile, the melt pool boundaries in the plane-YZ are also dependent on the dimensions of the melt pool. As shown in 9c, in the cross section perpendicular to the scanning direction, the melt pool of sample-A has the smallest width, while the melt pool in sample-C has the largest width. As a result, the melt pool boundaries change drastically with the rotating scanning direction in different layers in sample-A, while the melt pool boundaries in sample-C are much flatter, as shown in Fig. 9c and Fig. 9f. The frequently changed melt pool boundaries in sample-A indicate that the direction of the temperature gradient in sample-A is highly inhomogeneous. The direction of ITGs rotates together with the scanning direction, while the change in VTGs is not significant as they are nearly parallel with the build direction (Z axis).

The complex temperature gradient profile in NiTi sample-A enables the growth of grains with various orientations resulting in different

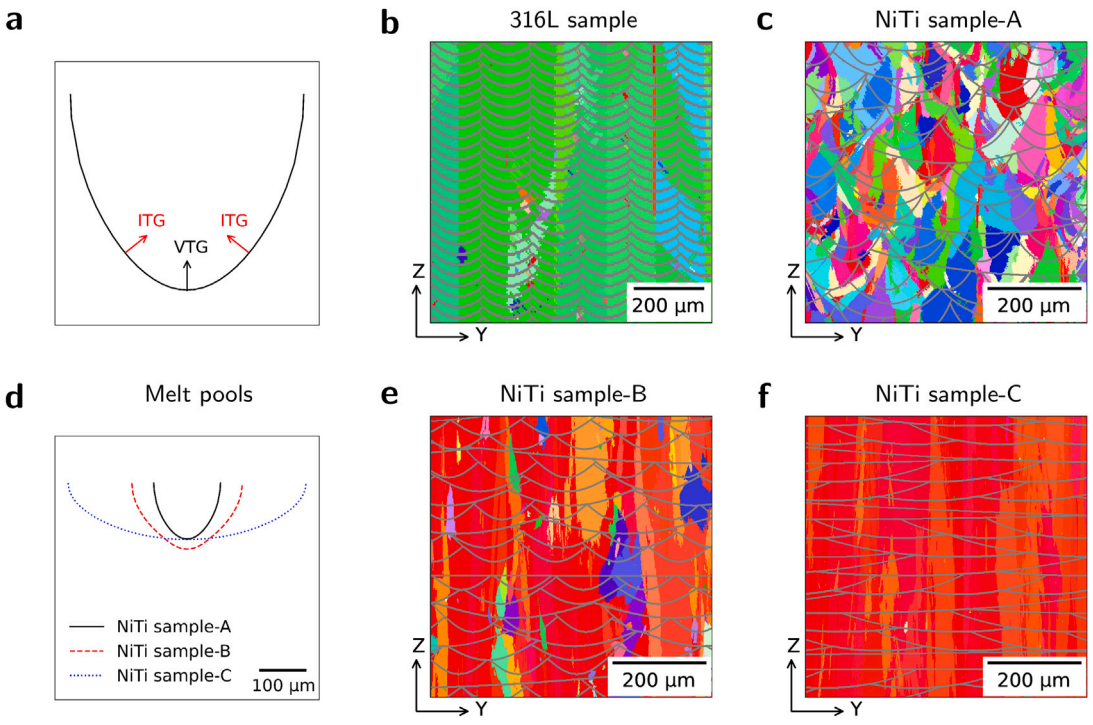

Fig. 9. Selection of preferential orientations with temperature gradients. **a** The temperature gradients in the lower part of a melt pool are divided into two types: vertical temperature gradient (VTG) and inclined temperature gradient (ITG). **b** Comparison of the melt dimensions in the three NiTi samples. **c**, **d**, **e** and **f** The melt pool boundaries superimposed on microstructure in selected regions in plane-YZ for the 316L sample, NiTi sample-A, NiTi sample-B and NiTi sample-C, respectively. Local temperature gradients are perpendicular to the melt pool boundaries, which select preferential orientations.

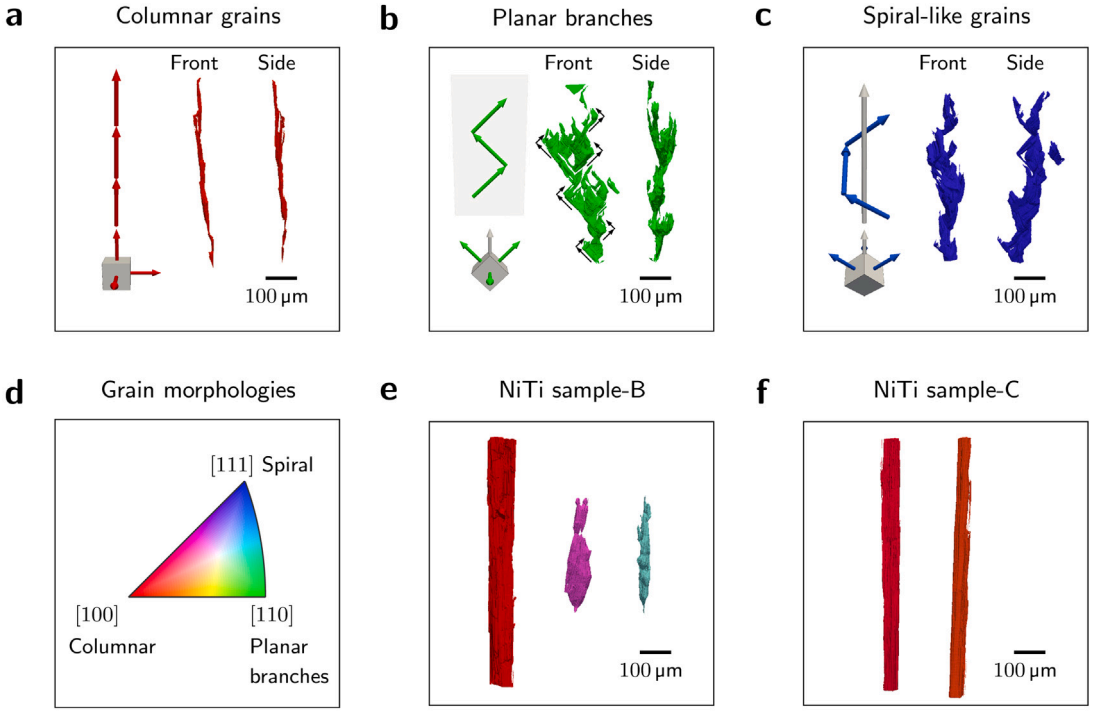

Fig. 10. Orientation-dependent grain morphologies in NiTi samples. Grain morphologies in NiTi sample-A: **a** columnar grains, **b** planar branches and **c** spiral-like grains. **d** Relation between grain morphology and orientation in NiTi sample-A. **e** Grain morphologies in NiTi sample-B. **f** Grain morphologies in NiTi sample-C.

grain morphologies, as shown in Figs. 10a, 10b and 10c. The grain morphology is orientation dependent, as shown in Fig. 10d. Grains with ⟨100⟩ ∥ Z orientations typically exhibit a columnar or trunk-like morphology (Fig. 10a); grains with ⟨110⟩ ∥ Z orientations tend to have planar branches (Fig. 10b); grains with ⟨111⟩ ∥ Z orientations display a spiral-like structure (Fig. 10c). For grains with other orientations, a mixture of the spiral-like structure and planar branches is commonly observed. Similar branch-like grain morphologies have been observed experimentally [40]. The dependence of the grain morphology on the orientation can be explained by grow patterns, which are constructed

with the effective ⟨100⟩ crystallographic directions, namely, the ⟨100⟩ crystallographic directions that are not perpendicular to the Z axis. In NiTi sample-A, a VTG or a ITG may be aligned with a specific ⟨100⟩ crystallographic direction. However, a temperature gradient perpendicular to the Z axis cannot be found in the multi-pass temperature gradient profile. Therefore, orientations with ⟨100⟩ ∥ Z, ⟨110⟩ ∥ Z and ⟨111⟩ ∥ Z have one, two and three effective ⟨100⟩ crystallographic directions, leading to different growth patterns, as shown in Figs. 10a, 10b and 10c. Note the growth patterns depicted in Fig. 10 represent basic units of growth patterns, from which more complex growth patterns can be generated. Grains with ⟨100⟩ ∥ Z exhibit a linear growth pattern (Fig. 10a); grains with ⟨110⟩ ∥ Z display a zigzag growth pattern (Fig. 10b); grains with ⟨110⟩ ∥ Z have a spiral-like growth pattern (Fig. 10c). For grains with other orientations, a mixture of the zigzag growth pattern and the spiral growth pattern is expected. Grains grow larger when their growth pattern aligns with the local temperature gradients. The linear growth pattern of grains with ⟨100⟩ ∥ Z can be satisfied with VTG. However, due to the frequently changed melt pool boundaries, the VTG-dominated region is either thin or short, leading to a thin columnar morphology (Fig. 10a) or a short trunk-like morphology. The zigzag growth pattern can be facilitated by ITGs of various melt pools, leading to the formation of planar branches. Similarly, the spiral growth pattern can be supported by ITGs, resulting in the formation of spiral-like grains. Note that the majority of grains in NiTi sample-A, excluding those aligned with ⟨100⟩ ∥ Z or ⟨110⟩ ∥ Z, or orientations lying in between, exhibit spiral-like features. The spiral feature becomes stronger as the orientation approaches ⟨111⟩ ∥ Z. This leads to the formation of polygon shapes in plane-XY, as shown in Fig. 4d. In summary, the texture in NiTi sample-A is weak due to the complex temperature gradient profile, which facilitates the growth of grains with various orientations.

The melt pool in NiTi sample-B is wider than the melt pool in NiTi sample-A, while the hatch distance in NiTi sample-B is the same as the hatch distance in NiTi sample-A. Consequently, the melt pool boundaries in NiTi sample-B are flatter, with VTGs predominating across the majority of the simulation domain. This favors the growth of ⟨110⟩ ∥ Z grains in a columnar shape, as shown in Fig. 10e, leading to the formation of a ⟨100⟩ fiber texture. The finding that flatter melt pool boundaries promotes the formation of ⟨100⟩ texture is consistent with the predictions by Rolchigo et al. [26] based on a texture selection angle. In NiTi sample-B, grains with globally unfavorable orientations can only find their growth pattern satisfied within a limited domain, often resulting in strip-like shapes, as shown in Fig. 10e. In NiTi sample-C, the melt pool is even wider than the melt pool in NiTi sample-B. In this case, the vast majority of the simulation domain is dominated by VTGs. This leads to a stronger ⟨100⟩ fiber texture in NiTi sample-C compared to NiTi sample-B. Most grains in NiTi sample-C are in columnar shapes.

5. Conclusion

In this work, an improved three-dimensional (3D) cellular automata (CA) model has been developed. By analytically calculating the growth length and employing a multi-level capture algorithm, the time-step dependence of CA simulations has been effectively eliminated. The employment of large times steps, combined with a pass-by-pass sparse temperature algorithm, has led to a significant acceleration in the simulation of crystallographic textures and grain morphologies in additively manufactured metallic materials. With experimental validations, our optimized 3D CA model demonstrates its robustness as a tool for microstructure prediction. This model represents a significant advancement in efficient microstructure prediction for additive manufacturing.

Through the analysis of both simulated and experimental results, this research uncovers the governing mechanisms behind the evolution of textures and grain morphologies. The resultant microstructure and texture are controlled by temperature gradients originating from melt pools across different layers. In a domain dominated by vertical temperature gradients, ⟨100⟩ ∥ Z grains are favorable to grow, leading to a ⟨100⟩ fiber texture. In a domain dominated by inclined temperature gradients, the microstructure and the texture are dependent on the interactions between temperature gradients of the melt pools. Orientation-dependent growth patterns can be satisfied locally (NiTi sample-A) or globally (316L steel sample), leading to different microstructures and textures. It is thus a potential method to achieve desired microstructures and textures by tuning temperature gradients through a control of the melt pool shape and scanning strategy.

CRediT authorship contribution statement

Xiaohui Liang: Writing – original draft, Software, Investigation, Data curation, Conceptualization. **Jianing Zhu:** Writing – review & editing, Writing – original draft, Resources, Methodology, Investigation, Formal analysis, Conceptualization. **Vera Popovich:** Writing – review & editing, Supervision. **Marcel Hermans:** Writing – review & editing, Supervision. **Ian Richardson:** Writing – review & editing, Supervision, Funding acquisition. **Cornelis Bos:** Writing – review & editing, Resources, Project administration, Conceptualization.

Declaration of competing interest

The authors declare that they have no known competing financial interests or personal relationships that could have appeared to influence the work reported in this paper.

Acknowledgments

This research was carried out under project number T17019 g in the framework of the Research Program of the Materials innovation institute (M2i) (www.m2i.nl) supported by the Dutch government.

Appendix A. Supplementary data

Supplementary material related to this article can be found online at https://doi.org/10.1016/j.addma.2024.104622.

Data availability

Data will be made available on request.

References

[1] R. Li, H. Li, H. Pan, D. Xie, J. Zhang, D. Fang, Y. Dai, D. Zhao, H. Zhang, Achieving exceptionally high strength in binary mg-13gd alloy by strong texture and substantial precipitates, Scr. Mater. 193 (2021) 142–146.
[2] C.L. Pavithra, B.V. Sarada, K.V. Rajulapati, M. Ramakrishna, R.C. Gundakaram, T.N. Rao, G. Sundararajan, Controllable crystallographic texture in copper foils exhibiting enhanced mechanical and electrical properties by pulse reverse electrodeposition, Cryst. Growth Des. 15 (9) (2015) 4448–4458.
[3] H. Bunge, Texture and magnetic properties, Textures Microstruct. 11 (1970).
[4] R.C. Reed, The Superalloys: Fundamentals and Applications, Cambridge University Press, 2008.
[5] J.-N. Zhu, K. Liu, T. Riemslag, F.D. Tichelaar, E. Borisov, X. Yao, A. Popovich, R. Huizenga, M. Hermans, V. Popovich, Achieving superelasticity in additively manufactured ni-lean niti by crystallographic design, Mater. Des. 230 (2023) 111949.
[6] I. Bitharas, N. Parab, C. Zhao, T. Sun, A. Rollett, A. Moore, The interplay between vapour, liquid, and solid phases in laser powder bed fusion, Nature Commun. 13 (1) (2022) 2959.
[7] T. DebRoy, H. Wei, J. Zuback, T. Mukherjee, J. Elmer, J. Milewski, A.M. Beese, A. d. Wilson-Heid, A. De, W. Zhang, Additive manufacturing of metallic components–process, structure and properties, Prog. Mater. Sci. 92 (2018) 112–224.
[8] A. C. F. on Additive Manufacturing Technologies and A. C. F. on Additive Manufacturing Technologies. Subcommittee F42. 91 on Terminology, Standard Terminology for Additive Manufacturing Technologies, Astm International, 2012.

[9] T. Debroy, W. Zhang, J. Turner, S.S. Babu, Building digital twins of 3D printing machines, Scr. Mater. 135 (2017) 119–124.
[10] M.-S. Pham, B. Dovgyy, P.A. Hooper, C.M. Gourlay, A. Piglione, The role of side-branching in microstructure development in laser powder-bed fusion, Nature Commun. 11 (1) (2020) 749.
[11] T. Mukherjee, T. DebRoy, A digital twin for rapid qualification of 3D printed metallic components, Appl. Mater. Today 14 (2019) 59–65.
[12] Y. Huang, T.G. Fleming, S.J. Clark, S. Marussi, K. Fezzaa, J. Thiyagalingam, C.L.A. Leung, P.D. Lee, Keyhole fluctuation and pore formation mechanisms during laser powder bed fusion additive manufacturing, Nature Commun. 13 (1) (2022) 1170.
[13] J.A. Koepf, M.R. Gotterbarm, M. Markl, C. Körner, 3D multi-layer grain structure simulation of powder bed fusion additive manufacturing, Acta Mater. 152 (2018) 119–126.
[14] Y. Lian, Z. Gan, C. Yu, D. Kats, W.K. Liu, G.J. Wagner, A cellular automaton finite volume method for microstructure evolution during additive manufacturing, Mater. Des. 169 (2019) 107672.
[15] D.-R. Liu, S. Wang, W. Yan, Grain structure evolution in transition-mode melting in direct energy deposition, Mater. Des. 194 (2020) 108919.
[16] R. Shi, S.A. Khairallah, T.T. Roehling, T.W. Heo, J.T. McKeown, M.J. Matthews, Microstructural control in metal laser powder bed fusion additive manufacturing using laser beam shaping strategy, Acta Mater. 184 (2020) 284–305.
[17] K. Teferra, D.J. Rowenhorst, Optimizing the cellular automata finite element model for additive manufacturing to simulate large microstructures, Acta Mater. 213 (2021) 116930.
[18] T. Carozzani, C.-A. Gandin, H. Digonnet, Optimized parallel computing for cellular automaton–finite element modeling of solidification grain structures, Modelling Simul. Mater. Sci. Eng. 22 (1) (2013) 015012.
[19] C.-A. Gandin, M. Rappaz, A 3D cellular automaton algorithm for the prediction of dendritic grain growth, Acta Mater. 45 (5) (1997) 2187–2195.
[20] S. Chen, G. Guillemot, C.-A. Gandin, Three-dimensional cellular automaton-finite element modeling of solidification grain structures for arc-welding processes, Acta Mater. 115 (2016) 448–467.
[21] M. Yaghoobi, S. Ganesan, S. Sundar, A. Lakshmanan, S. Rudraraju, J.E. Allison, V. Sundararaghavan, Prisms-plasticity: An open-source crystal plasticity finite element software, Comput. Mater. Sci. 169 (2019) 109078.
[22] Y. Lian, S. Lin, W. Yan, W.K. Liu, G.J. Wagner, A parallelized three-dimensional cellular automaton model for grain growth during additive manufacturing, Comput. Mech. 61 (2018) 543–558.
[23] O. Zinovieva, A. Zinoviev, V. Romanova, R. Balokhonov, Three-dimensional analysis of grain structure and texture of additively manufactured 316L austenitic stainless steel, Addit. Manuf. 36 (2020) 101521.
[24] M. Rolchigo, B. Stump, J. Belak, A. Plotkowski, Sparse thermal data for cellular automata modeling of grain structure in additive manufacturing, Modelling Simul. Mater. Sci. Eng. 28 (6) (2020) 065003.
[25] M. Rolchigo, S.T. Reeve, B. Stump, G.L. Knapp, J. Coleman, A. Plotkowski, J. Belak, ExaCA: A performance portable exascale cellular automata application for alloy solidification modeling, Comput. Mater. Sci. 214 (2022) 111692.
[26] M. Rolchigo, J. Coleman, G.L. Knapp, A. Plotkowski, Grain structure and texture selection regimes in metal powder bed fusion, Addit. Manuf. 81 (2024) 104024.
[27] E.J. Schwalbach, S.P. Donegan, M.G. Chapman, K.J. Chaput, M.A. Groeber, A discrete source model of powder bed fusion additive manufacturing thermal history, Addit. Manuf. 25 (2019) 485–498.
[28] X. Li, W. Tan, Numerical investigation of effects of nucleation mechanisms on grain structure in metal additive manufacturing, Comput. Mater. Sci. 153 (2018) 159–169.
[29] W. Kurz, B. Giovanola, R. Trivedi, Theory of microstructural development during rapid solidification, Acta Metall. 34 (5) (1986) 823–830.
[30] A. Zinoviev, O. Zinovieva, V. Ploshikhin, V. Romanova, R. Balokhonov, Evolution of grain structure during laser additive manufacturing. simulation by a cellular automata method, Mater. Des. 106 (2016) 321–329.
[31] D.-C. Tsai, W.-S. Hwang, A three dimensional cellular automaton model for the prediction of solidification morphologies of brass alloy by horizontal continuous casting and its experimental verification, Mater. Trans. 52 (4) (2011) 787–794.
[32] Y. Zhang, J. Zhang, Modeling of solidification microstructure evolution in laser powder bed fusion fabricated 316L stainless steel using combined computational fluid dynamics and cellular automata, Addit. Manuf. 28 (2019) 750–765.
[33] M. Rolchigo, R. LeSar, Application of alloy solidification theory to cellular automata modeling of near-rapid constrained solidification, Comput. Mater. Sci. 163 (2019) 148–161.
[34] A. Pineau, G. Guillemot, D. Tourret, A. Karma, C.-A. Gandin, Growth competition between columnar dendritic grains–cellular automaton versus phase field modeling, Acta Mater. 155 (2018) 286–301.
[35] X. Ao, H. Xia, J. Liu, Q. He, Simulations of microstructure coupling with moving molten pool by selective laser melting using a cellular automaton, Mater. Des. 185 (2020) 108230.
[36] M. Diehl, P. Eisenlohr, C. Zhang, J. Nastola, P. Shanthraj, F. Roters, A flexible and efficient output file format for grain-scale multiphysics simulations, Integr. Mater. Manuf. Innov. 6 (2017) 83–91.
[37] R. Hielscher, H. Schaeben, A novel pole figure inversion method: specification of the MTEX algorithm, J. Appl. Crystallogr. 41 (6) (2008) 1024–1037.
[38] O. Andreau, I. Koutiri, P. Peyre, J.-D. Penot, N. Saintier, E. Pessard, T. De Terris, C. Dupuy, T. Baudin, Texture control of 316L parts by modulation of the melt pool morphology in selective laser melting, J. Mater. Process. Technol. 264 (2019) 21–31.
[39] S. Kou, Welding Metallurgy, vol. 431, (446) New Jersey, USA, 2003, pp. 223–225.
[40] Z. Sun, S.-P. Tsai, P. Konijnenberg, J.-Y. Wang, S. Zaefferer, A large-volume 3D ebsd study on additively manufactured 316L stainless steel, Scr. Mater. 238 (2024) 115723.